Integrating Acoustic Measurements and Microstructural Analysis on the Bebertal Sandstone to Predict the State of Stress Before Deformation

Annisa Rachmi Trahwiwit

For the degree:

Master of Science in Geophysics at Utrecht University

5621526

Project duration: March – September, 2017

Universiteit Utrecht

Abstract

This case study presents an experimental investigation of predicting the state of stress before deformation by integrating acoustic measurements and microstructural analysis on dry Bebertal sandstone. Three dry cubic Bebertal sandstone goes through two different stress path with three different maximum differential and hydrostatic stress under true triaxial stress at room temperature. Acoustic measurements were measured while conducting the deviatoric and hydrostatic stress method. The aim was to determine whether the hydrostatic stress can create the same stress before deformation. After all three samples went through deviatoric stress, three deformed samples based on the acoustic measurement shows different stress points when deformed. Hydrostatic stress was applied to the samples after deviatoric stress. Unfortunately, the hydrostatic method was unable to predict the state of stress before deformation. The deformed samples are then digitized to map out cracks spread throughout the samples. There was a correlation between maximum differential stress with number of cracks where the higher the maximum differential, the higher the number of cracks residing in the sample.

Keyword: Bebertal sandstone, deviatoric stress, hydrostatic stress, crack mapping, differential stress

Table of Contents

List of Figures

List of Tables

Chapter 1. Introduction

The Groningen gas field located in the northern part of The Netherlands is known to be one of the largest gas reservoir in the world. The field was discovered in 1959 and gas production began in 1963. Since then, they have produced approximately 2115 billion m3 (bcm) out of the original 3000 bcm in place (Thienen-Visser and Breunese, 2015). However, since the 1990's seismic activity in the, otherwise tectonically inactive, area started to increase. Approximately one thousand minor earthquakes have been registered between 1991 and 2013 (KNMI, 2013a). Between 1991 and 2001, seismicity was roughly constant, at approximately five events per year (Thienen-Visser and Breunese, 2015), but since then has increased. The largest event was detected near Huizinge, in August 2012 with a magnitude of 3.6 on the Richter scale, causing the most damage to date (KNMI, 2013b, Thienen-Visser and Breunese, 2015). This development has made understanding what is happening in the Groningen reservoir, in response to gas production, and how it drives induced seismicity even more pressing.

It is believed that the surface subsidence and induced seismicity seen in the Groningen gas field are driven by compaction at the reservoir level. Gas production reduces the gas pressure P_f in the reservoir, such that the reservoir rocks feels the effective weight of the overburden formations, i.e. the effective vertical stress σ_e increases as $\sigma_e = \sigma_v - P_f$, where σ_v is the vertical stress exerted by the overburden formations. As a result, the reservoir will start to compact. Initially this compaction may be elastic, but if the stresses acting on the grain framework making up the reservoir rock become too large, permanent deformation may occur. Differential compaction occurring across faults in the reservoir can lead to shear stress concentrations across the faults, which may lead to fault reactivation and induced seismicity. Therefore, to assess the driving force for surface subsidence and induced seismicity, it is key to understand and predict reservoir compaction. Reservoir compaction might have a strong connection with reservoir depth, composition, basin and production history, and material properties are various factors that might strongly be effect reservoir compaction. (Hol et al., 2015). Various factors that is responsible of stress changes in the reservoir such as pressure solution creep, grain cracking, pore collapse, and shear failure (Hol et al., 2015).

In order to understand the mechanisms driving compaction, laboratory experiments and numerical simulations need to be performed by employing the true in-situ conditions, meaning actual reservoir stress, pressure, and temperature conditions. While the reservoir gas pressure and temperature of the Groningen gas field are known from downhole measurements, the in-situ state stress is still poorly

constrained (NAM, 2016). One potential tool to assess the in-situ stress state is by performing true triaxial experiments coupled by measuring P- and S-wave velocities (Kern, 2011). Elastic wave velocity is strongly affected by crack density and crack orientations of the rock, which may be affected by pre-existing or (production-) induced crack damage (Browning et al., 2015). Via controlled true triaxial experiments, along suitable stress paths, it should be possible to determine the three principal stresses at which existing crack damage is closed and no new cracks have been introduced yet, i.e. the in-situ state of stress of the rock at the time of retrieval. Such To do these tests, we have could be performed on material available from the reservoir formation obtained prior to production (SDM-1 well) and in 2014/15 (ZRP-3A), i.e. from the depleted reservoir (NAM, 2016).

However, since the available Slochteren sandstone material for such tests is limited, three rock samples originated from the same formation as the Groningen gas reservoir was used to conduct the experiment. The three rock samples undergone two different stress ($\sigma_1 > \sigma_2 = \sigma_3$) path, deviatoric stress and hydrostatic stress ($\sigma_1 = \sigma_2 = \sigma_3$). The initial purpose of implementing deviatoric stress was to initiate damage and re-create new cracks aside pre-existing cracks. Hydrostatic stress was used to close the new existing cracks created from the deviatoric stress stage in order to determine the three principal stresses at which crack are closed. Is it possible to detect the previous state of stress after the material has experienced core damage with the Vp and Vs measurements? Measuring the elastic waves helped in identifying at what stress point new cracks form and close. In addition, microstructure analysis of the deformed Bebertal samples was performed to analyze the crack density and crack orientation.

Chapter 2: True triaxial Compression: apparatus and experimental procedure

2.1 Sample material and geological setting

The rock samples originated from Bebertal outcrops located in Flechtingen High, North Germany which are aeolian fluvial Upper Rotliegend sandstones (Fischer et al., 2012). Lithic subarkoses, rounded to well-rounded grains and well-sorted laminae set throughout the aeolian-fluvial Rotliegend sediments which are known for deeply buried Upper Rotliegend sandstones on the southern side of the Nothern German Basin (Kulke et al., 1993; Gast et al., 2010; Fischer et al., 2012). Saline lake sediments from the central part (Gast, 1991), fluvial and aeolian sediments located at the basin margins (Ziegler, 1990) makes up the Roliegend basin fill (Schröder et al., 1995)

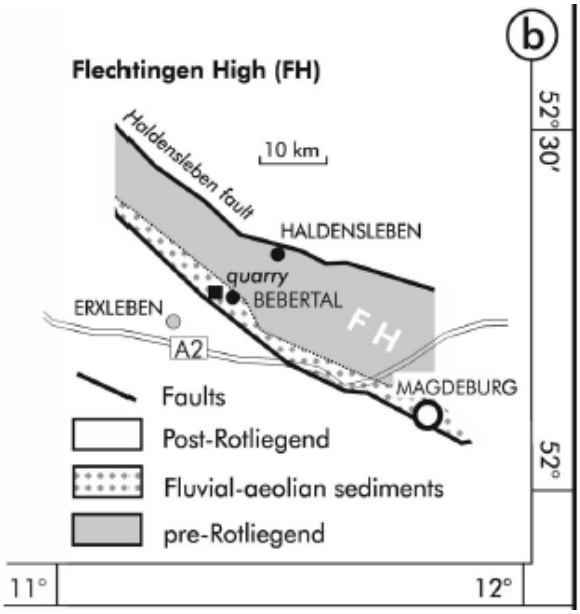

Figure 1 The samples originated on the FH which are the northernmost outcrops of sediments of Upper Rotliegend sandstones (Fischer et al., 2012).

The rock samples were made in to ~5x5x5 cm cubes which was then sent to Christian – Albrechts University in Kiel to be made fit to the machine by a technician, Andreas Fehler, where the samples would be experimented on under guidance of Dr. H. Bahadur Motra.

Figure 2 Three cubes of the Bebertal sandstone before applying deviatoric and hydrostatic stress (left) KB-1b, (middle) KB-1a, and (right) KB-1c.

2.2 True triaxial compression apparatus and experimental procedure

Velocity measurement of P and S wave were measured by using the multi-anvil apparatus located at the Christian – Albrechts University in Kiel under the guidance of Dr. H. Bahadur Motra. The apparatus uses the ultrasonic transmission technique (Kern, 1982) to measure the seismic velocity using transducers with a frequency of 2 and 1 MHz for P and S waves, respectively (Kern et al., 1997).

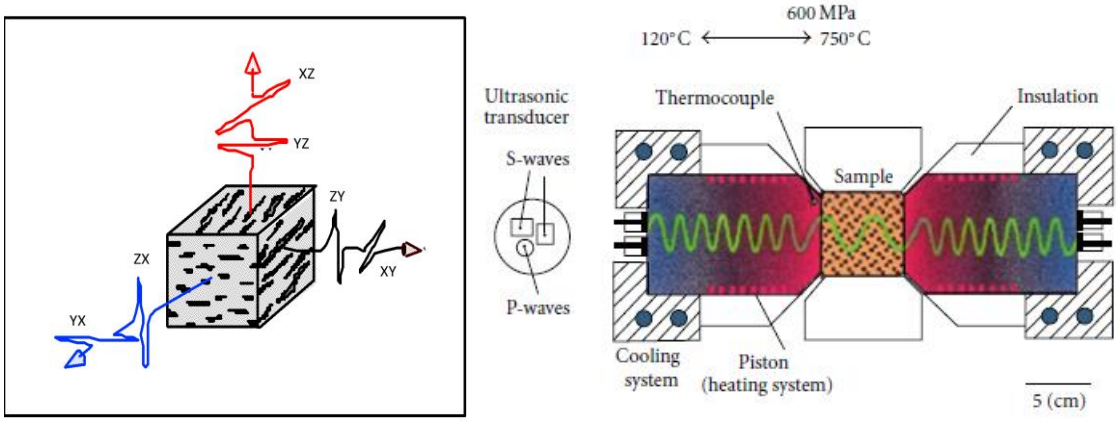

Figure 3 Reference system for velocities in the cube sample (left)(Kern, 2011), the transducer-piston-sample arrangement in multi-anvil pressure apparatus (right)(Kern, 2011).

The P and S wave velocities are measured simultaneously along the X, Y and Z directions as a function of pressure and temperature. In this case, the experiment was conducted under room temperature. Shear wave experiences splitting when wave travels through an anisotropic medium resulting two propagating waves where one component propagates in the 'fast' direction with a relatively fast velocity and the other component travels through an orthogonal plane with a relatively slow velocity (Menke and Levin, 2003). Hence, in the multi-anvil apparatus there are two orthogonally polarized transducers positioned perpendicular to each other specifically to measure the shear wave splitting (Figure *3*). One set of measurement consisted of 9 measured velocities, three P wave velocities and six S wave velocities, along with the volume change of the sample. The deformation of the sample is measured based on the change of length from the piston displacement (Kern et al., 2001).

Figure 4 Six pistons from the sample is in process of being pressurized by six pyramidal pistons in three orthogonal direction.

At the beginning of the experiment, the sample reached a nearly-hydrostatic stress induced by the pressure caused by the six pyramidal pistons in the three orthogonal directions to ensure the pistons are in contact with the sample (Kern et al., 1997). The error tolerance of the time measuring is ±5 ns and accuracy is to be higher than ±0.5% (Kern et al., 1997).

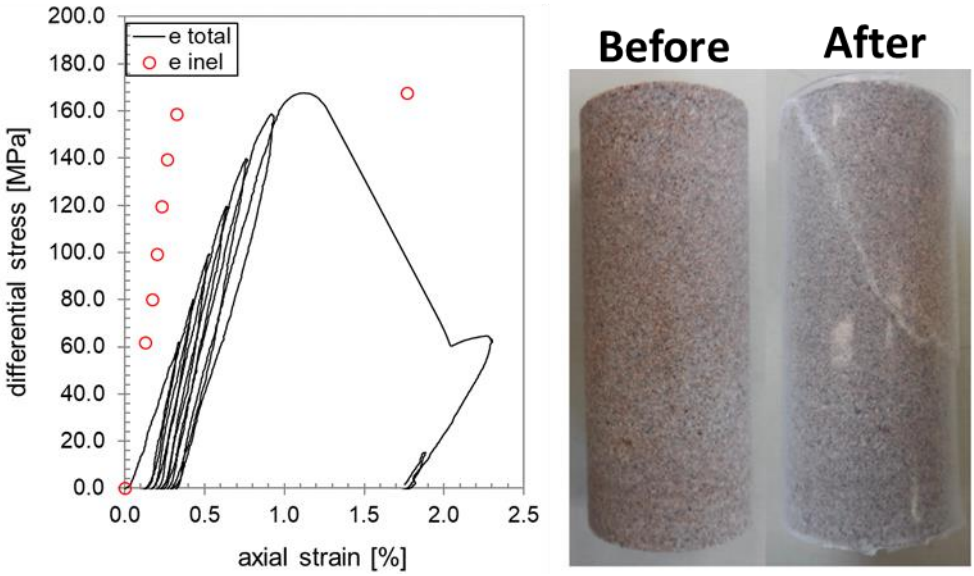

Figure 5 A separate experiment was conducted on a cylindrical rock sample originated from the same rock as the three cubic rock samples. The diagram displays the result of the experiment, axial strain (%) over differential stress. The image of the sample is before and after deformation.

A separate experiment which was performed in Utrecht University conducted by a PhD student of Utrecht University, R. P. J. Pijnenburg MSc., was used to investigate the yield point of a dry Bebertal sandstone by applying conventional triaxial stress. The sample originated from the same source rock as the three cubic rock samples and was shaped cylindrical. The state of the sample was in a dry condition to relate to the three main samples. The purpose of this experiment was not only to find the yield point, but to choose three different differential stresses ($\sigma_1 - \sigma_3$) to be compared in the next step of the experiment.

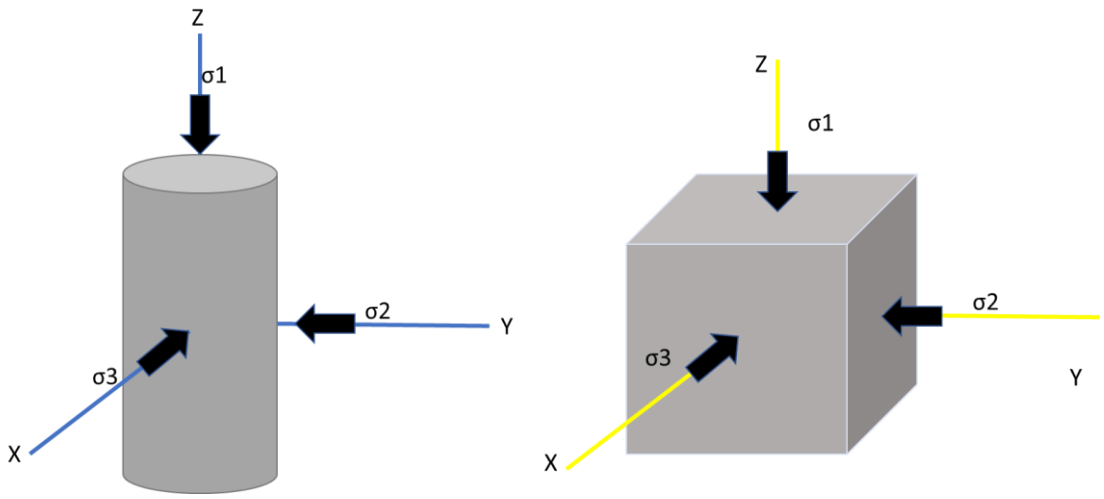

Figure 6 An illustration of the direction for each stress applied on the cylindrical (left) and cubic (right) sample.

The maximum principal compressive stress, σ_1 was increased slowly while the intermediate, σ_2, and minimum, σ_3, was constantly the same. Initially the volume decreased caused by closure of some primary pores and cracks as compaction is increased (Alkan et al.,2007; Klein et al., 2001). After increasing stress at a certain point, the maximum stress was decreased for the purpose to see the change in axial strain. The strain had a significant change from 0.3 % to 1.7% when the differential stress peak was 167.1 MPa. The significant increase of strain indicates the inception of dilatancy. By visual inspection, the sample shows a clear shear localization (Figure *5*).

To refer to the conventional triaxial apparatus stress, three maximum differential stress were chosen for the true triaxial stress, 80, 120 and 140 MPa. The lowest differential stress, 80 MPa was based on another experiment conducted by R.J.P Pijnenburg MSc., where he used a wet sandstone instead of dry. The result was quite different to the dry sandstone where initially crack starts to grow at a differential stress of 80MPa. Hence, the lower limit of differential stress for the true triaxial apparatus was based on the wet sandstone, 120 MPa and the highest limit was based on the conventional triaxial stress performed on dry sandstone, 140 MPa.

The cubic samples as stated before was experimented in Kiel with a different apparatus than done for the conventional triaxial stress. The steps that were taken was slightly different to the conventional triaxial stress. Unlike the conventional triaxial stress experiment, the maximum stress, σ_1, was increased continuously without decreasing σ_1. In between stress, an average time span of 19 minutes was used to observe the deformation measured by the pistons. Alongside the maximum stress, intermediate (σ_2) and minimum stress (σ_3) was increased until both had reached 15 MPa and stayed constant while σ_1 was

increased. The purpose was to let the sample be in equilibrium state before having to increase more stress. This was to be cautious of creep that might happen during the experiment.

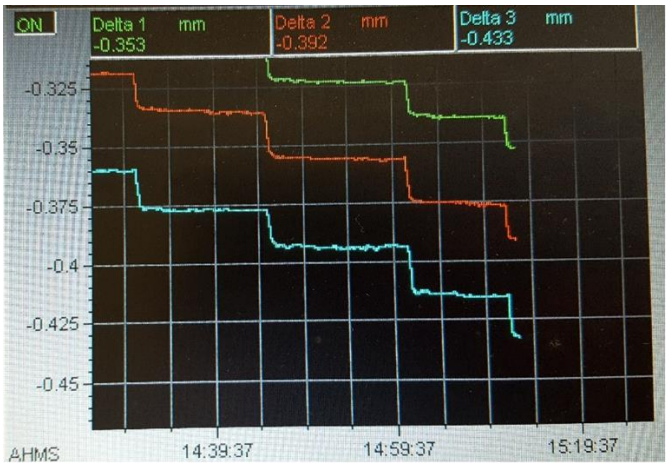

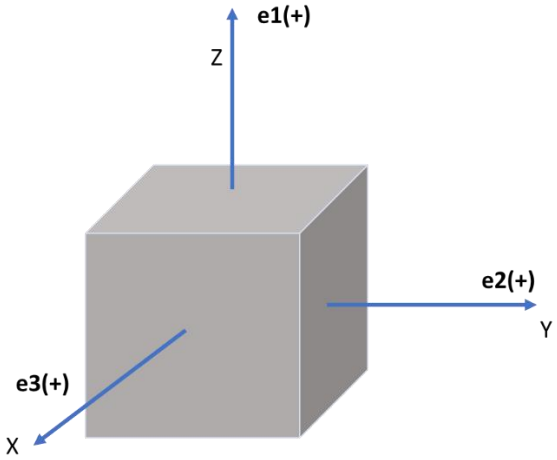

Figure 7 Monito for observing deformation based on the change of length of the pistons displacement, axial strain. The Y-axis of the monitor is the displays the length displacement and the X-axis is the time of measurement. Delta 1 is the Z-direction, Delta 2 is the Y-direction and Delta 3 is the X-direction. An illustration of the placement of the strain in the measurement (right).

Three cubic samples at the beginning of the experiment went through the deviatoric stress method where $\sigma_1 > \sigma_2 = \sigma_3$. All three stresses were increased every two MPa until all three reached 15 MPa. At 15 MPa, σ_2 and σ_3 stayed constant at 15 MPa ($\sigma_2 = \sigma_3$) while σ_1 continues to increase every 10 MPa until the assigned maximum differential stress for each sample was reached. After the confined pressure reached the assigned value, σ_1 decreased differently for different rock samples. There was no reason behind the difference in stress reduction for each rock. The average amount of time in between reducing stress was 13 minutes.

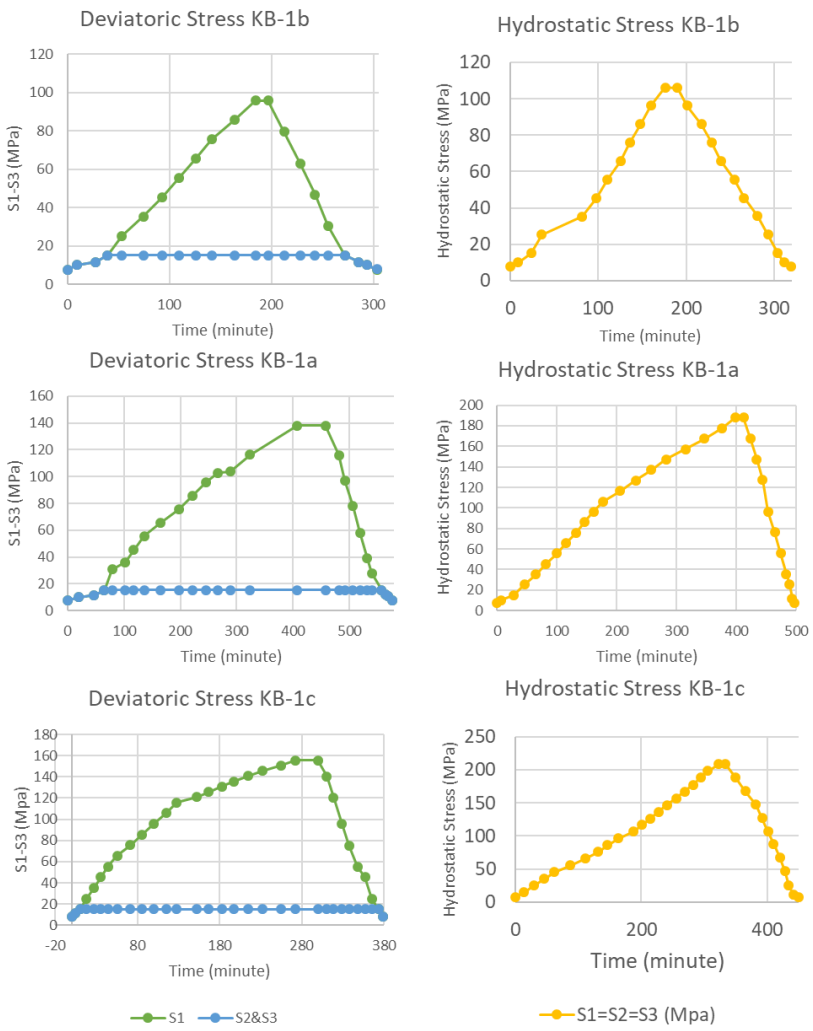

Figure 8 The deviatoric stress diagrams (left) for sample KB - 1b, KB - 1a and KB - 1c, differential stress (MPa) versus time (minute) diagrams where the green dotted lines are $\sigma_1 - \sigma_3$ and the blue dotted lines are $\sigma_2 = \sigma_3$; The hydrostatic stress diagrams (right) displays hydrostatic stress ($\sigma_1 = \sigma_2 = \sigma_3$) versus time (minute) represented by the yellow dotted lines ($\sigma_1 = \sigma_3 = \sigma_4$).

After deviatoric stress was applied to the samples, hydrostatic stress was tested to the same specimen. Similar steps were taken, except that $\sigma_1 = \sigma_2 = \sigma_3$. Hence, all three stress were increased with the same value until it reached the assigned maximum stress. Identical to the deviatoric stress, the first few increased stresses were 2 – 5 MPa until 15 MPa was reached, then was continued by increasing 10 MPa. The average time span for the samples to be in an equilibrium state was 18 minutes. As it reached the assigned maximum stress, all three stress were reduced every 20 MPa with an average time span of 11 minutes.

For both deviatoric and hydrostatic stress method, compressional and shear wave velocities were measured in X, Y, and Z as a function of pressure at room temperature. The measurement was done the moment when the sample is in a stable state, before the stress was increased even further. The P and S wave are denoted by Vp_i and Vs_{ij} where the first subscript *i* of Vp and Vs indicates the direction of the wave propagation, while *j* of Vs*i* indicates the polarization direction.

2.3 Microstructural methods

2.3.1 Image Preparation

Crack mapping and porosity estimation of the sample were needed to be prepared in such a way where the cracks and porosity could be measured with minimum error. The un-deformed and deformed samples had different type of sections where the un-deformed and deformed were thin and thick section, respectively, however this decision had no effect to the end results.

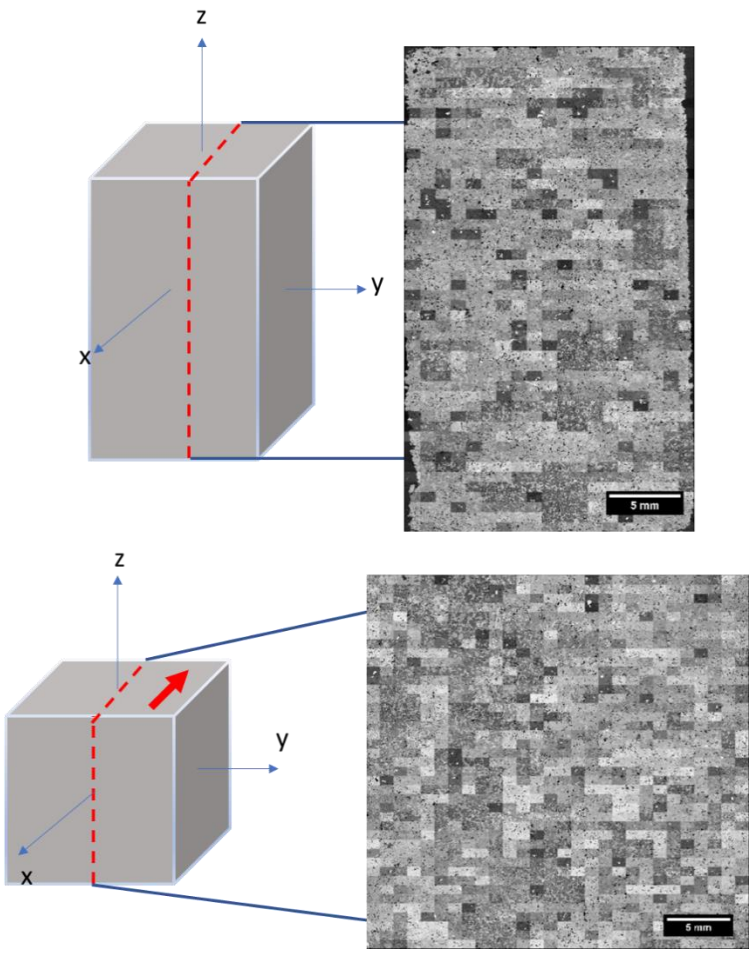

Figure 9 The illustration of the area of where the thin and thick sections were cut out from the arranged blocks. The thin section was done on the un-deformed sample (top) and the thick section was assigned to the deformed samples (bottom). The red arrow on the deformed samples was to give an idea of the orientation of where the sample was placed on the multi-anvil apparatus.

The un-deformed and deformed samples were cut in the middle of the block to avoid minimum external damages such as sample preparation, excessive stress, etc. One point that stands out was excessive stress which in this case is only specified to the deformed samples. All six pistons are in contact with six surfaces of the block where the surfaces received extra amount of stress compared to the inner part of the block. Hence, to avoid difficulties in crack interpretation to the requested section, the cut was parallel to the Z-direction. Consequently, the surfaces that face the Z-direction are the only surfaces that might have damage due to extra stress mounted upon it. The reason behind the cut parallel to the Z-direction was due to the deviatoric stress where σ_1. The red arrow illustrated in Figure 9 represents the orientation of where the sample was placed on the multi-anvil apparatus which was also taken in to account to direct how the cut should be done.

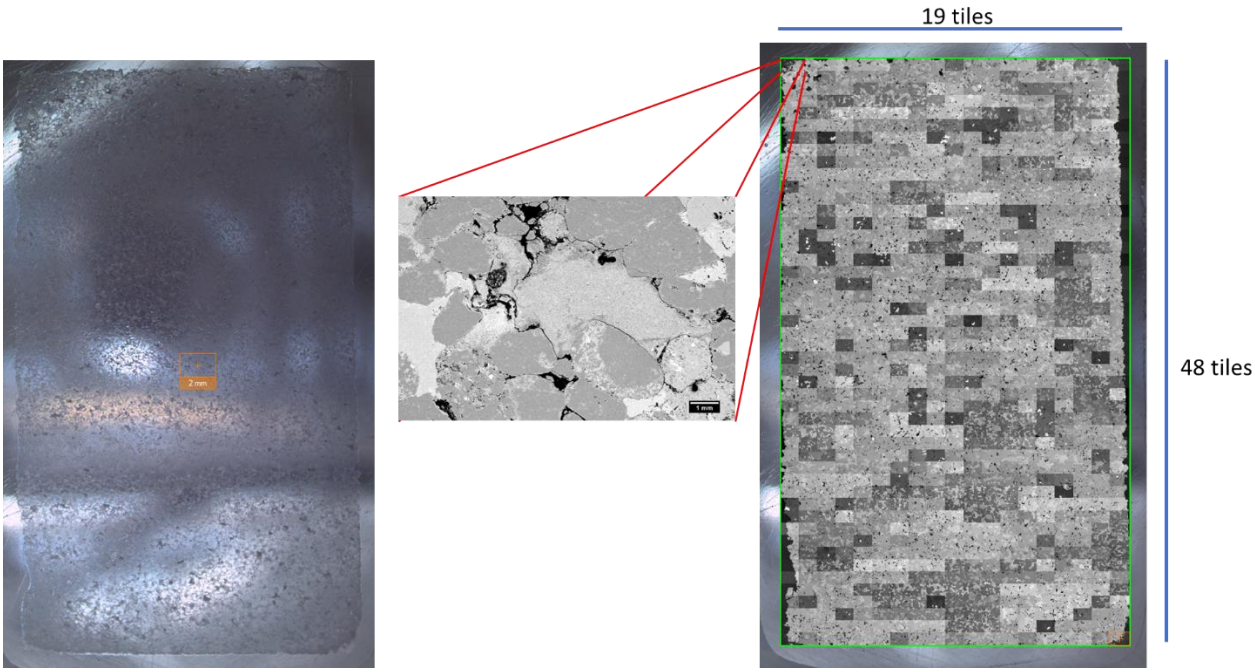

Figure 10 The thin section of the un-deformed sample was coated in palladium mixed platinum (left), the backscattered electron images (BSE) in form of a mosaic tile (middle), the backscattered electron images (BSE) in form of the whole thin section (right). The results are given in mosaic tiles which eventually be stitched together. In total, there are at total of 912 mosaic tiles.

The thin and thick sections were then coated with palladium mixed platinum to be prepared for the scanning process by using the Scanning Electron Microscope done in Utrecht University. The images used were the BSE images. Each section of the images was mapped using a concentric backscatter detector by using a horizontal field with 1.18 mm per mosaic tile. Each mosaic tile was generated using an acceleration using an acceleration voltage of 10 kV and beam current of 1.6 nA, employing a dwell time of 1 or 3 µs.

For the un-deformed sample, the mosaics consist of 19 (columns) to 48 tiles (rows). The deformed sample, KB-1a has 1148 mosaic tiles consisting of 27 columns and 43 rows; Kb-1b has 2460 tiles with 41 columns and 60 rows; KB-1c has 1161 tiles, 27 columns and 43 rows. The mosaic tiles were stitched using ImageJ with a tile overlap of 10%. Specifically, for KB-1b, the stitching was done in to two parts because the computer was unable to stitch 2460 tiles simultaneously.

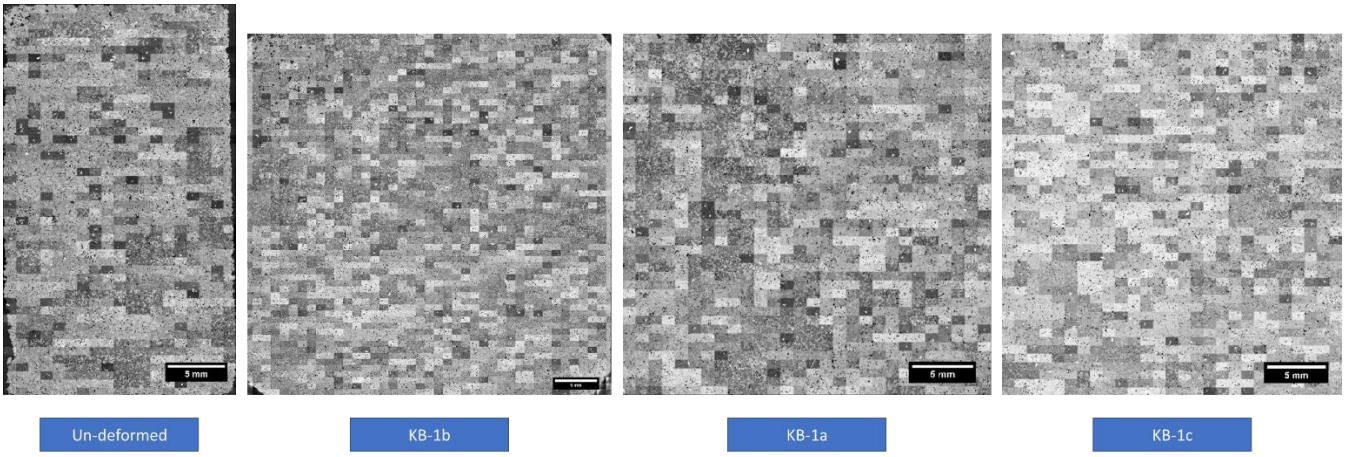

Figure 11 The thin and thick section BSE images that were stitched together using the ImageJ program with a tile overlap of 10%.

2.3.2 Crack mapping and porosity estimation

Crack mapping and porosity estimation was done to un-deformed and three deformed samples. The purpose of crack mapping is to quantify cracks spread out throughout the sample and to estimate the crack density of the sample. Crack is defined as a singular line represented by black pixels within the grain, intragranular cracks. The difficulty of mapping cracks is due to the quality of the BSE images which is unambiguously to identify. Crack angle is also important to measure to be able to give an idea of the overall crack angle throughout the sample. The angle was measured using ImageJ which applied Feret's diameter. Feret's diameter or known as maximum caliper measures the longest distance between two points along the appointed boundary. The angle given by this measurement goes from 0 – 180 degrees.

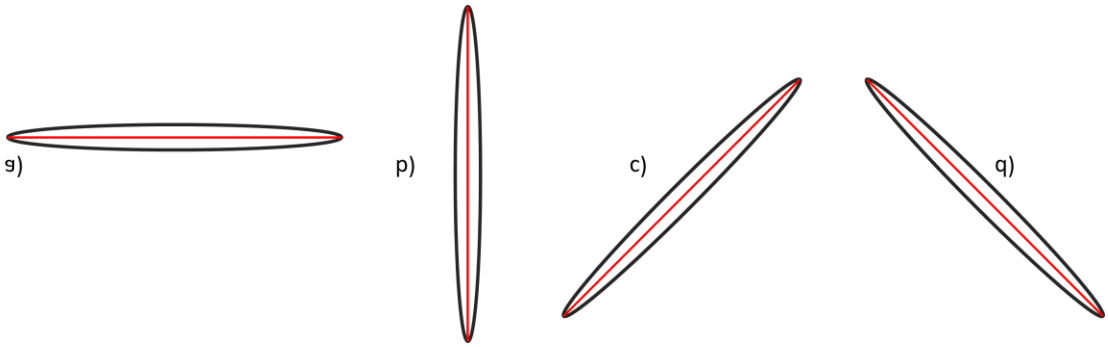

Figure 12 How Feret's diameter would measure cracks which are positioned in different angles. a) 0°, b)90°, c) 45°, and d) 135°.

The crack density is calculated by applying this formula:

$$Crack\ density = \frac{Total\ Cracks}{(Bulk\ fraction - (porosity\ x\ bulk\ fraction))}\ x\ 100\%$$

Total cracks are estimated by counting cracks that have been mapped throughout a disclosed area. This is done to avoid areas of the image where there might be damages which cause cracks to appear within the grain. Bulk fraction is the area of the disclosed part of the image, where each sample has different bulk fraction. Porosity is calculated by configuring the image where ImageJ can distinguish between pore and solid materials.

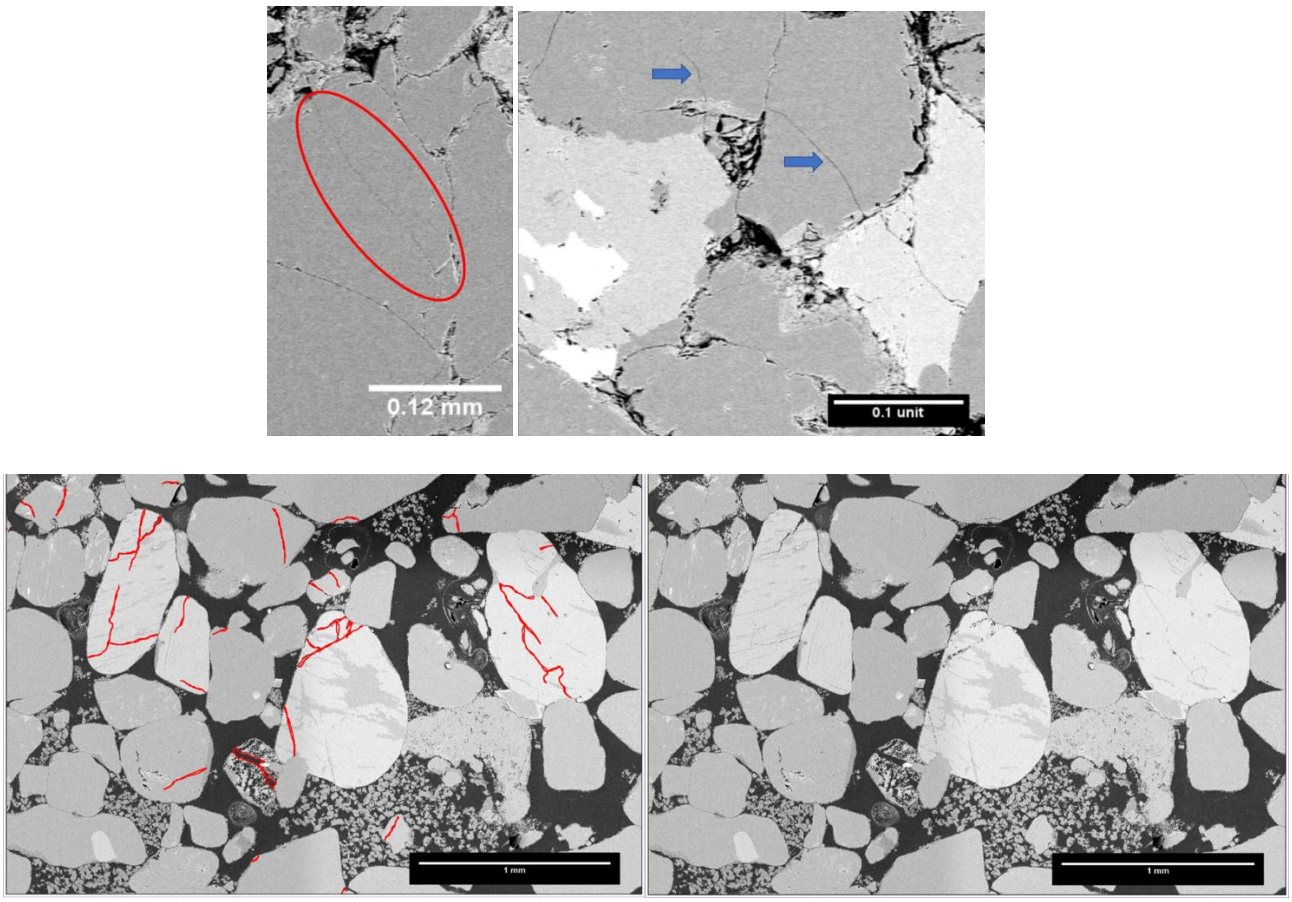

Figure 13 Image on the top left is an image taken from KB-1a where the red circle surrounds a crack present within the grain and the top right image was from KB-1c, the blue arrows point out cracks present within the grain. The bottom left image is the image taken from the Slochteran sandstone, taken from the Groningen gas field, where the cracks are mapped in red and the image on the bottom right is the original image without the cracks mapped.

Pore fraction was calculated by configuring the images in such a way that pore and solid can be calculated separately. Due to the different contrast in grey caused by noises, such as scratches, dust, dirt, etc. which appeared on the BSE images, the images had to go through a process where the grey contrast is similar to one mosaic image to another mosaic image, contrast-leveling. This was done by using Photoshop where one image was taken as a reference of the grey contrast and the contrast was applied to all images. The images were then stitched with ImageJ. For ImageJ to be able to differentiate pore and solid fraction, the image had to be in black and white where black is identified as pore and white as solid.

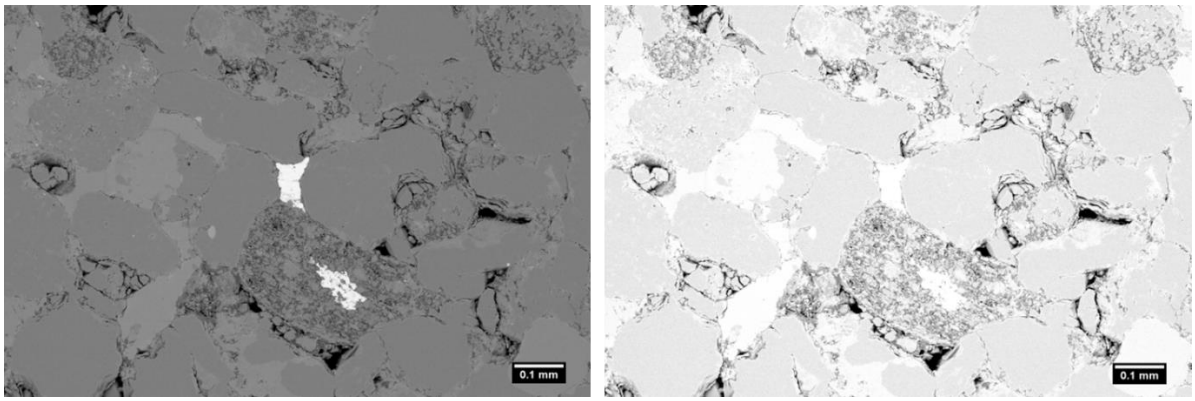

Figure 14 Image on the left is the BSE image of sample KB-1c before it went through contrast-leveling while the image on the right is the processed image.

After synchronizing the grey contrast and stitching the mosaic tiles in to one image, the BSE image went through various steps to obtain binary image by using ImageJ. Because of unnecessary details such as crack outlines, the image needs to be blurred to extract fundamental information which in this case is the pore and solid fractions. The image went through a filter, Gaussian blur with a radius of 2, to obscure irrelevant information (crack outlines). After Gaussian blur, the full image is then thresholded with the Otsu Threshold to finally gain the binary image file. From the binary image, ImageJ calculates the percentage of pore based on the black pixels throughout the image and the white pixels for the bulk fractions.

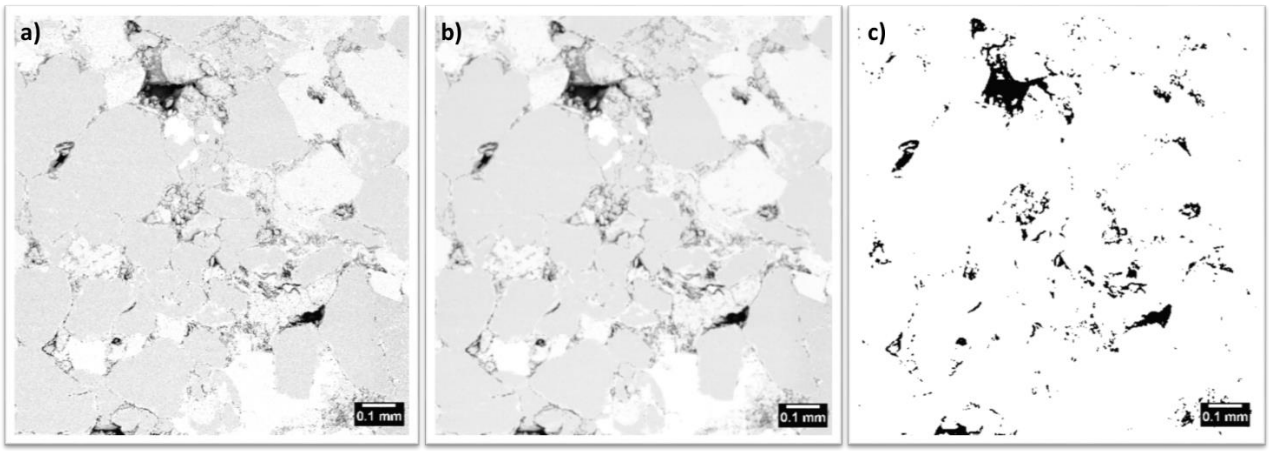

Figure 15 a) A section of the image of KB-1c after contrast-leveling process, b) a section of KB-1c after applying Gaussian Blur with a radius of 2, c) the binary image of the section of KB-1c after implementing Otsu Threshold.

Based on the quality of the SEM images, cracks were quite difficult to map because not only the quality of the images, but also whether the assumed cracks are really cracks or just alteration caused by weathering or chemical reactions with other minerals? Cracks mapped in this case study are cracks caused

by deformation. In which to be certain whether these cracks are caused by mineral alteration, such as plagioclase or K-feldspar, or purely deformation, Energy Dispersive X-Ray (EDX) analysis was done on KB-1a assuming all four sample has the same mineral content.

The sample was coated with palladium mixed platinum, then was placed in the EDX Tabletop machine located in Utrecht University. The EDX analysis generated spectra showing peaks which corresponds to the elements making up the true composition of the sample. Because EDX uses an electron beam, the beam is directed to the chosen area. The machine does not identify the whole mineral, but captures the elements. The selected minerals were not randomly chosen, but were picked based on the grey contrast displayed in EDX.

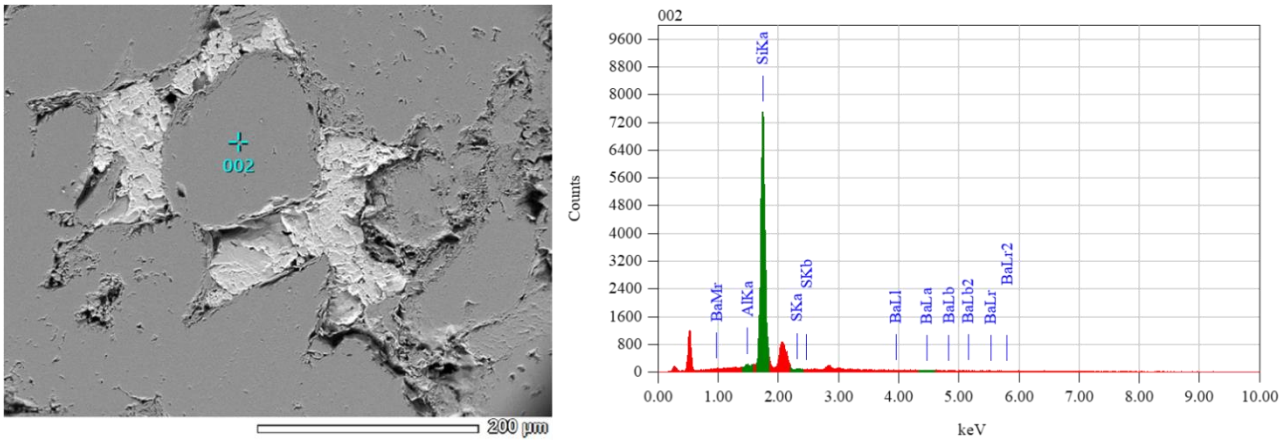

Figure 16 The image displays the image from the EDX analysis where X marks the spot of the beam (right). The diagram consists of peaks that corresponds to the elements which makes up the true composition. In this case, silica shows a high peak compared to the rest of the elements.

EDX analysis provide quantitative analysis to help in quantifying the elements in percentage form. In Figure 15 based on the quantitative analysis, the beamed area consists of 53.23% Oxide (O), 45.82% Silica (Si), 0.67% Sulfur (S), and 0.29% Barium (Ba). Ratio alone, Silica and Oxide are the two elements composing the mineral. The rest of the elements, Barium and Sulfur are elements that came from the surrounding of the focused area which had been. Mineral identification was not just based on EDX analysis alone, but also depend on crystal shape. The crystal shape varies for one mineral in just one image, moreover if there are several images. However, there is always a distinct shape which can differentiate that mineral to another mineral. To ensure the composition of the sample, the analysis was done 49 times. Based on the EDX tabletop analysis, four minerals were detected, quartz, calcite barite, and K-feldspar.

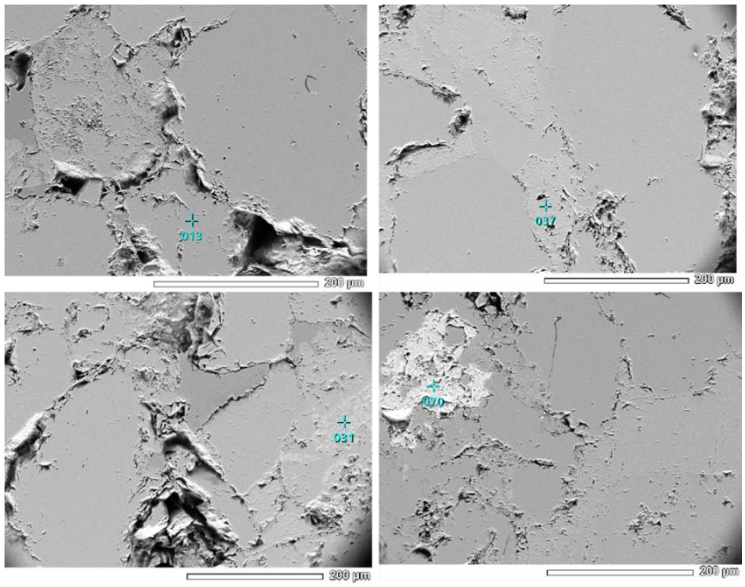

Figure 17 Four images with different mineral content the assigned mineral is pointed by a blue plus sign :(top left) quartz, (top right) calcite, (bottom left) feldspar, (bottom right) K-feldspar.

The result from the EDX analysis is used to pursue further on to the quantitative analysis which is to quantify the content of each minerals in the sample assuming all three samples have the same percentage content. Stated before, to quantify the content of each mineral, Multi – Otsu Thresholding method (Liao et al., 2001) is to separate the difference in grey scale. Roughly based on eye-sight alone, there is 5 different kind of shade of grey.

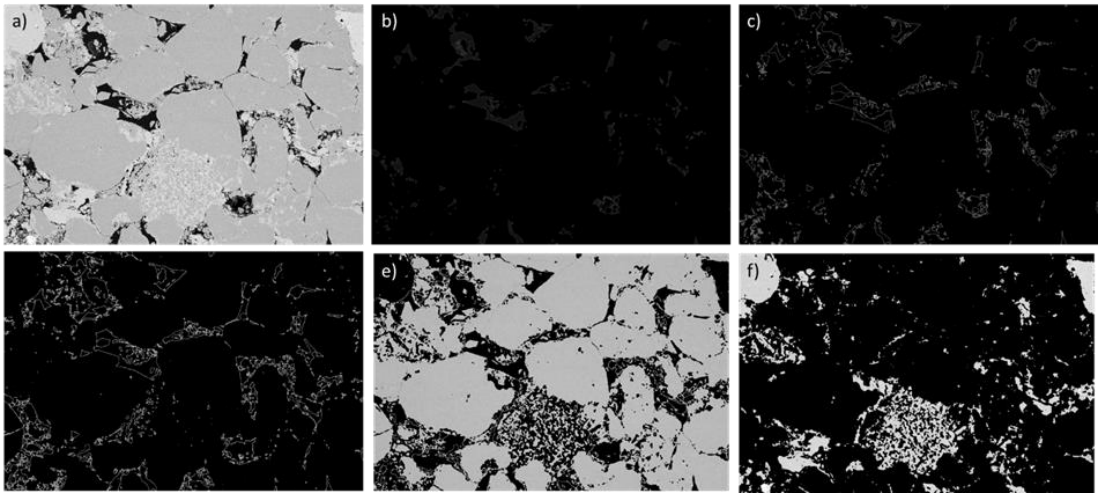

Figure 18 An example of the 5 layers of separation based on different shades of grey. a) original image, b) layer 1 assumes to be pores, c) layer 2 seems like clay, d) layer 3 also assume to clay, e) layer 4 is quartz, and f) layer 5 is a mixture between lithic fragments and K-feldspar.

A total of 670 out of 914 images was used to calculate the mineral content. The rest of the images that were left out, considered to be not suitable for the calculation due to noises on the images such as dust, hair, and scratches.

Chapter 3. Results

3.1 Mechanical data

3.1.1 Deviatoric stress stage

In deviatoric stress stage, the confining stress (σ_1) increases while the sample changes in volume, hence differential stress is $\sigma_1 - \sigma_3$. Whether it is significant or not is all based on the axial strains and volumetric strains results. The compaction in this case study is noted as positive, whereas extension is acclaimed negative.

Strain in general is calculated:

$$Strain\ (e) = \frac{\Delta L}{L}$$

Overall the strain in the Z-direction (e_1) the loading curve for KB-1b, KB-1a and KB-1c display inclination as axial stress was increased. In the result chapter, the change in strain will be defined in terms of 'lower' or 'higher'. The definition of 'higher' in the strain context is the value of the strain is higher which means that the length Z, Y, or X that direction has shortened. On the other hand, 'lower' is explained that the length parallel to the Z, Y, or X direction is extended. Meanwhile, in the volumetric strain context, 'higher' is defined as the sample experienced compaction while 'lower' means the sample went through dilation.

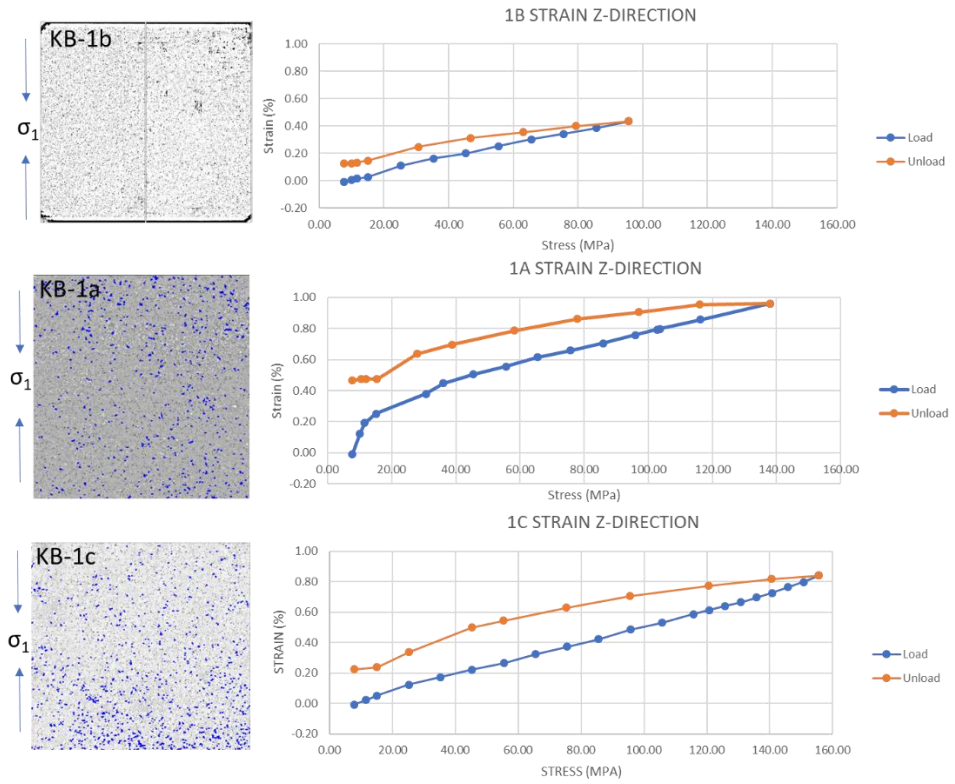

Figure 19 Microstructures (left) and axial strain e1 vs deviatoric stress plots (right) for KB-1b, KB-1a, and KB-1c. Orange dotted line represents the loading stress process and blue dotted line is the unloading process. For details on the microstructure see section 3.3.

Based on Figure 19, e_1 for all samples are likely to have the same pattern in the loading process where it increases, indicating shortening. When σ_1 is released slowly, elastic strain is released however permanent strain is apparent with the state of strain when fully unloaded. When σ_1 starts to decrease, the trend starts to show a similar pattern to the loading process implying elongation happening in the Z-direction. Despite of elongation occurring, there is a sign of slight permanent deformation of the sample shown in the end of the unloading process where the value is not the same as the start of the loading process. The axial strain of KB-1b and KB-1c in the load cycle has two trends, one starts from 8 to 15 MPa and the second trends starts from 15 until it reaches maximum stress. Even if KB-1a has two trends with the same start and end, the difference is the behavior of the first trend where at 8 to 15 MPa, the sample tends to shortens quicker than KB-1b and KB-1c.

Comparing the axial strain in the Z-direction of KB-1b from the beginning to the end of the loading process, the result is 51.9 times higher in value. The change from the start to the end of the unloading process is 0.7 times lower. Overall, axial strain has a change 15.5 times higher if we compare the start of the loading process to the ending of the unloading process. For KB-1a, the change in e_1 (loading process) is 113.4 times

higher compared to the start of the loading process and the ending process has slightly lower value compared to Kb-1b, however is still 0.5 times lower than the beginning of the unload. If we compare the beginning of loading to the end of unloading of KB-1a, the change of e_1 is 55.3 higher. The change of e_1 for KB-1c in the loading process is higher than KB-1b but slightly smaller than KB-1a, 99.1 higher than state at the beginning. While comparing the start and end process of unloading, change of e_1 is 0.7 lower similar to KB-1b and slightly higher to KB-1a. Overall, e_1 has changed 27.3 higher from its initial length, much smaller compared to KB-1b and KB-1a.

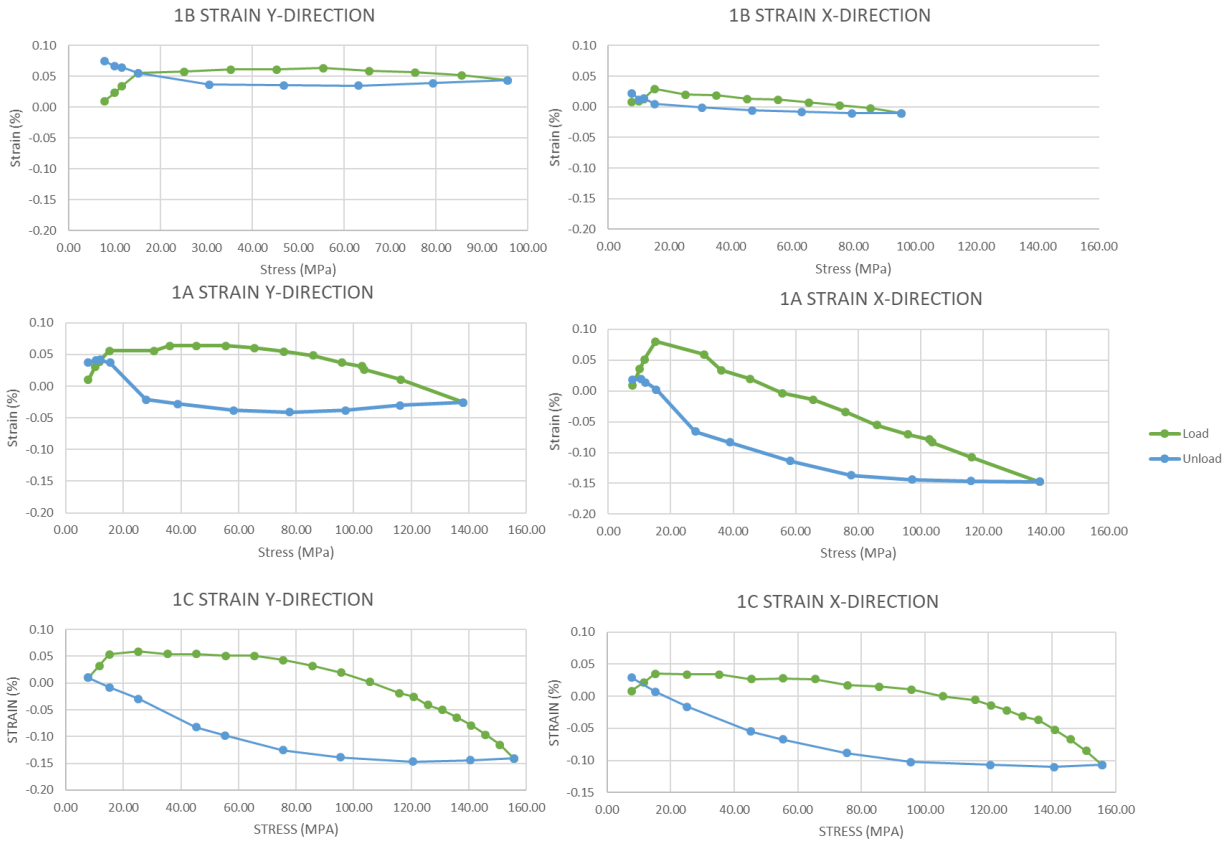

Figure 20 Axial strain e_2 (left) and e_3 (right) vs deviatoric stress on all three samples obtaining strain data in the Y and X direction where the green and blue dotted line are the loading and unloading curve, respectively.

Meanwhile, the behavior of the axial strain in the Y direction (e_2) and X direction (e_3) of KB-1b, KB-1a, and KB-1c for the loading and unloading process are different to e_1. The diagrams (*Figure 20*) show that the unloading curve does not have the same path pattern as the loading curve, however the change in axial strain is quite low compared to e_1. At 15 MPa, the curve tends to concave outwards in the load process while in the unload process, the curve for all samples concave inwards until the end of unloading process. At 15 MPa for all samples, when σ_1 was increased the sample is slowly extending shown in e_2 and e_3. In

the unloading process, e_2 and e_3 of KB-1b and KB-1a shows permanent strain. Kb-1c in e_2 apparently did not experience any shortening while in e_3, shortening is seen when fully unloaded.

The axial strain in the Y direction (e_2) and X direction (e_3) of KB-1b at the beginning of the loading process and the end of the unloading process have higher value than the beginning around 6.6 and 1.7 times higher. In the loading process for e_2 and e_3 of KB-1b, the changes are 3.5 and 2.2 times higher than the start of the cycle while in the unloading process, the differences are 0.7 and 3.1 times lower. Sample KB-1a shows a difference in e_2 and e_3 from the initial form to the end of the experiment (unloading process) are 2.8 and 1.1 times higher. In between cycles, after the loading cycle and before the start of the unloading cycle, e_2 and e_3 had higher value than the beginning of the loading cycle is 3.6 and 18 higher. While at the ending of the unloading cycle comparing to the start, the difference for e_2 and e_3 are 2.5 and 1.1 lower. Sample KB-1c's axial strain in the Y-direction (e_2) apparently did not change when compared to the beginning of loading and the end of the unloading cycle. Meanwhile, e_3 had changed to 2.5 times higher. The difference for the axial strain in the Y and X direction for the loading cycle are 15.3 and 13.8 higher. In the unloading cycle, the change in e_2 and e_3 are 1.1 and 1.3 lower.

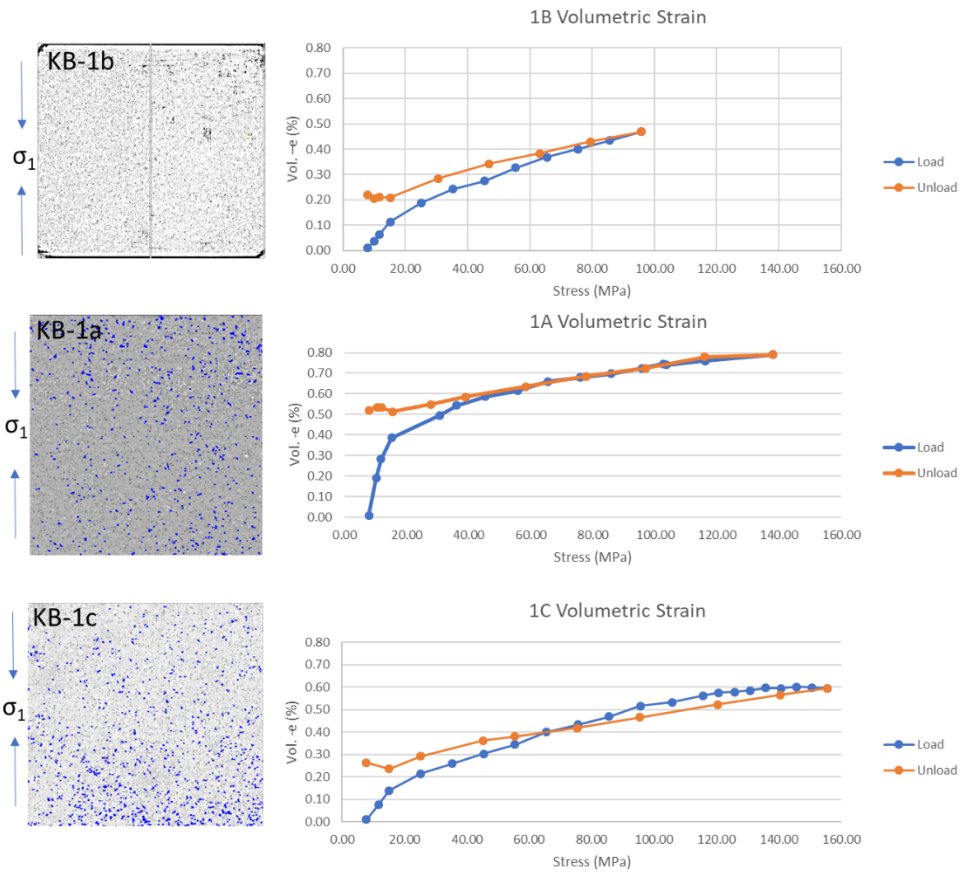

Figure 21 Microstructures (left) and volumetric strain vs deviatoric stress plots (right) for KB-1b, KB-1a, and KB-1c. Blue dotted line represents the loading curve and orange dotted line is the unloading curve.

At 8 to 15 MPa for the loading and the unloading process of KB-1b, KB-1a and KB-1c in the volumetric strain diagram happens to have a different trend that happens after 15 MPa. KB-1c apparently displays three different trends in the loading and the ending process. In the loading process the first trend starts from 8 to 15 Mpa behaving linearly, followed by a different trend which begins at 15 to 115 MPa, ended with a third trend, 115 to 155 MPa. Since the start of the unloading process begins at 155 MPa, thus the first trend starts off at 55 MPa to 155 MPa, continued by second trend at 15 to 55 MPa and ended with the third trend, 8 – 15 MPa. Sample KB-1a apparently shows a different behavior in curve pattern for the unloading process. At 58 to 97 MPa, the curve pattern of the unloading cycle seems to be in line with the loading curve, this behavior is quite different compared to KB-1b and KB-1c. In sample KB-1c, both the curve lines of the load and unload cycle intercepted into each other at 55 MPa. At that stress point, KB-1a does not show exactly an intercept, but after 58 MPa, the curve for the load and unload cycle deviated from being in line to each other.

The trend at 8 to 15 MPa where the sample was nearly in a hydrostatic state ($\sigma_1 = \sigma_2 = \sigma_3$) increased linearly for all samples, indicating that the samples are being compacted. Based on the end of the unload cycle, though elastic strain had a role in effecting the trend some of the strain was permanent as shown upon the volumetric strain of the samples which were higher than before the start of the experiment. The overall change of the volumetric strain for KB-1b, Kb-1a, and Kb-1c, comparing the initial state to the state after full unloading is 22, 53, and 26.4 times higher, respectively. The loading and unloading cycle for KB-1b is 47.7 higher and 0.5 lower compared to the beginning of each cycle, while KB-1a is 81 higher and 0.34 lower. Sample KB-1c has a change in the load cycle and unload cycle, 60.7 higher and 26.4 times lower, respectively.

3.1.2 Hydrostatic stress stage

Hydrostatic stress ($\sigma_1 = \sigma_2 = \sigma_3$) was applied to all three samples at room temperature. The change in axial strain of e_1 for sample KB-1b over hydrostatic stress in loading cycle is 33.9 times higher than the start of the cycle. In the unloading cycle, from maximum stress to fully unloaded (no applied stress), the change in strain is 0.8 lower. Overall, e_1 of KB-1b had deformed 6.1 higher from initial state to the state when fully unloaded of stress. KB-1a in the load cycle experienced change to 47.9 times higher than the initial state of the cycle, where in the unload cycle had changed to 0.7 lower. The total change is 13.2 times higher. The sample KB-1c has changed 60.5% in the load cycle and 0.9% in the end cycle. The sample has been deformed 6.2 times higher based on comparing the initial state to the state after stress has been fully unloaded from the sample.

Hydrostatic stress applied to the three samples appear to show no different behavior in terms of strain. One particular detail which caught attention is axial strain of the unloading process has higher values compared to the loading process this is presented by the curve of the unloading and the loading cycle. The unload curve is positioned higher in Figure 22 compared to the loading curve.

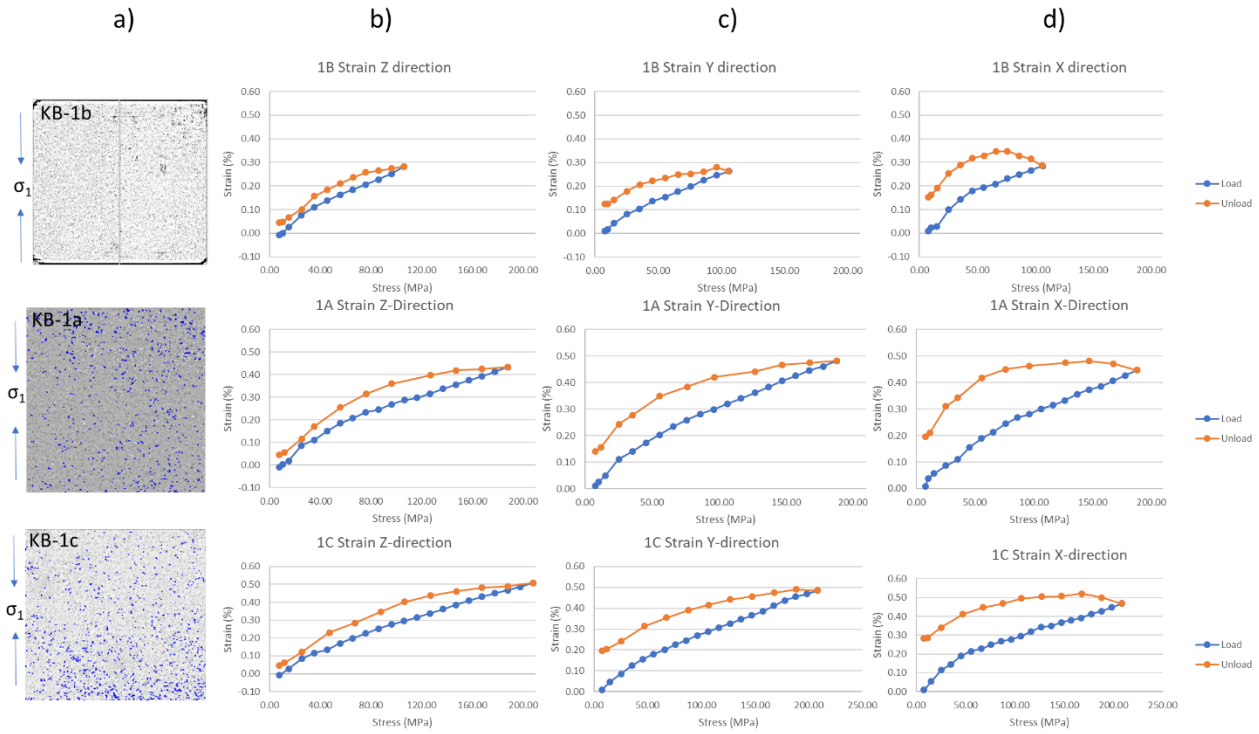

Figure 22 Microstructures (a) and axial strain e_1 (b), e_2 (c), and e_3 (d) vs hydrostatic stress plots for KB-1b, KB-1a, and KB-1c. Blue dotted line represents the loading stress process and orange dotted line is the unloading process.

Volumetric strain KB-1b compared from the beginning of load cycle to the end of the unload cycle has changed with a total of 32.2 times higher. In the load cycle, the volumetric strain of the sample deviated to 84.9 times higher while in the unload cycle, the sample changed 0.6 lower. As for sample KB-1a, in the load cycle the volumetric strain has changed 38.7 higher from the initial state to the state of stress being fully unloaded from the sample. The volumetric strain in the load process has a very high percentage in change compared to KB-1a, 139.8 times higher than the initial. In the unload process, the sample has changed 38.7 lower in volumetric strain. As for KB-1c with the highest maximum stress applied, the overall, load cycle and the unload cycle change are 53.3 higher, 150.1 higher, and 0.6 lower, respectively.

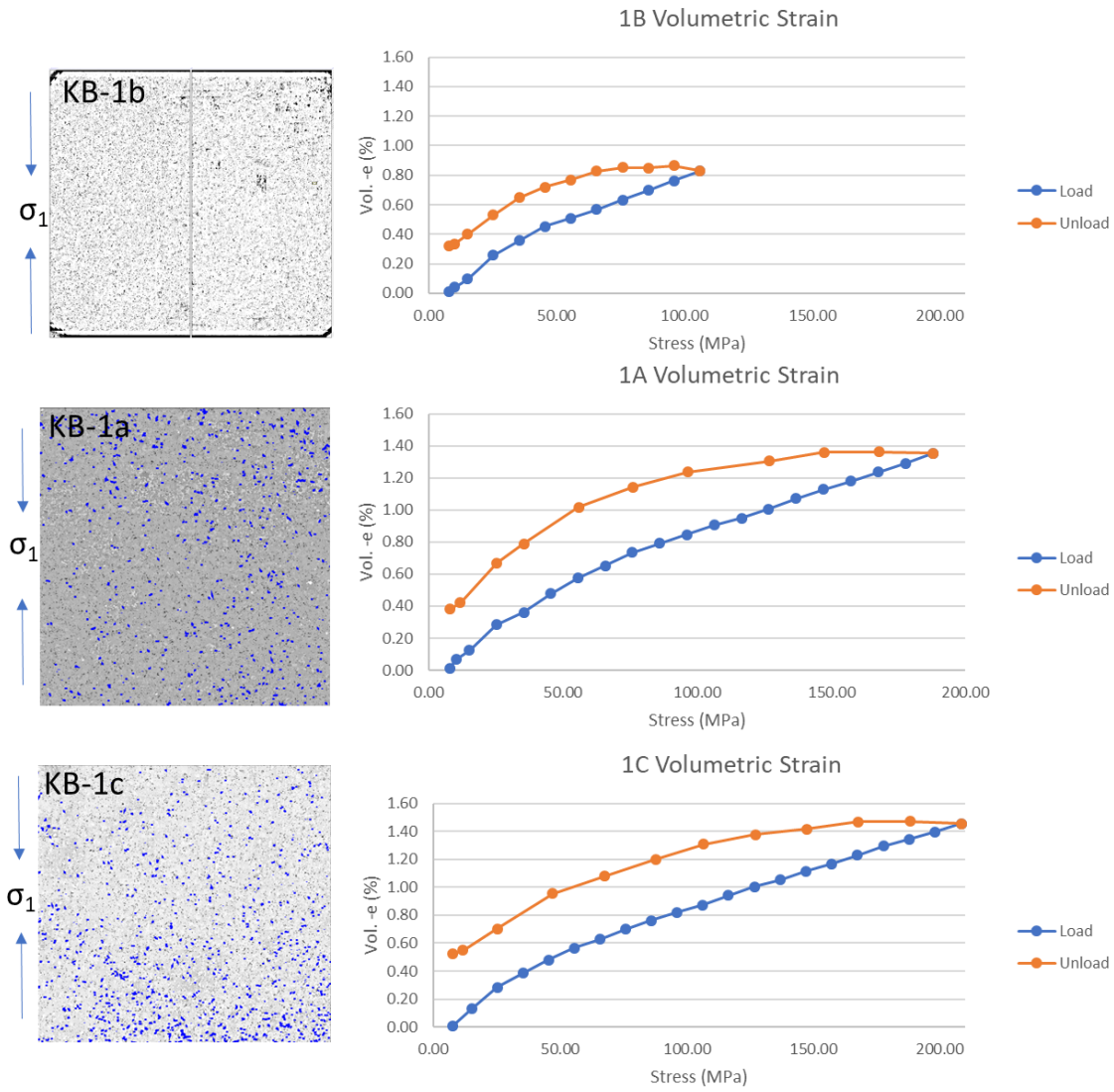

Figure 23 Microstructures (left) and volumetric strain vs hydrostatic stress plots (right) for KB-1b, KB-1a, and KB-1c. Blue dotted line represents the loading curve and orange dotted line is the unloading curve.

3.2 Wave velocity data

3.2.1 Deviatoric stress stage

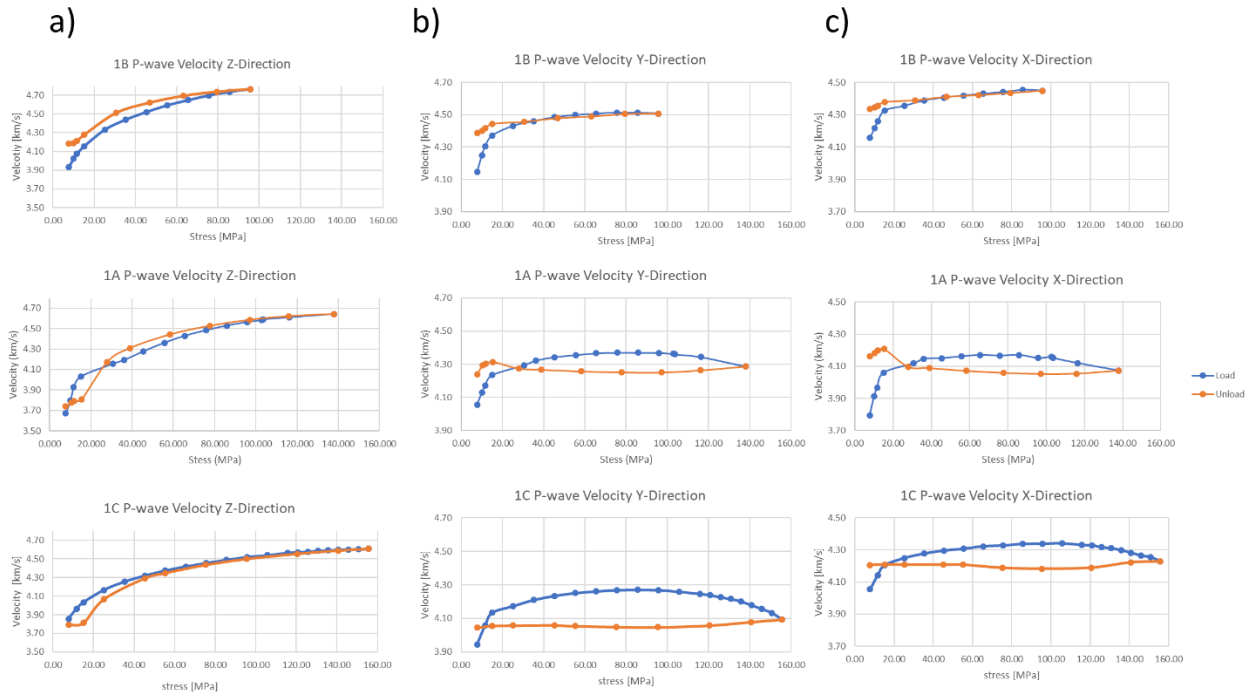

Figure 24 Compressional wave velocity Z-direction (b), Y-direction (c), and X-direction (d) vs deviatoric stress plots for KB-1b, KB-1a, and KB-1c. Blue dotted line represents the loading stress process and orange dotted line is the unloading process.

The P-wave measurement shows straightforward information in concern of permanent deformation of a rock. An increase of P-wave velocity in a sample indicates pore volume decreasing or cracks merely closing and decreasing in velocity implies cracks re-opening or new cracks developing within the rock.

The compressional wave velocity in the Z-direction, for all samples the unload curve of apparently shows similar pattern to the load curve. KB-1b and KB-1a at fully unloaded had a higher value compared to the initial state of the sample while as the KB-1c is slightly lower. Vp in the Z-direction increases over stress, however the rate of velocity increasing over stress is not always the same. Hence, trends could be seen on all three samples. KB-1b has two trends in the load curve, the first at 8 MPa to 15 MPa and the second 25 to 95 MPa, both trend shows an increase of velocity however second trend is not as much as the first trend. KB-1a and KB-1c have three trends in the load curve. For KB-1a, a linear trend which starts from 8 to 15 MPa, then deviates to a new trend 15 to 65 MPa, followed up by 75 to 138 MPa. There are three trends in the load curve of KB-1c, first trend 8 to 25 MPa, the second trend 35 to 105 Mpa and the third trend begins at 116 to 156 MPa. In KB-1b, the unloading curve, there happens to be two trends. The first one starts from 8 to 30 MPa and the second trend 30 to 80 MPa. KB-1 follows three trends, 8 MPa to 15

MPa, 15 to 27 MPa, and 38 to 138 MPa. KB-1c also has three trends, first trend 8 to 15 MPa, 15 to 45 MPa, and 55 to 156 MPa.

In the Y-direction, there happens to be similar trend that starts and ends at the approximately the same axial stress point. The first trend for all three samples starts from 8 to 15 MPa where the velocity increases, followed up by another trend 15 to 35 – 36 MPa, velocity increases but not as much as the first trend. The third trend of KB-1b and KB-1a in the load process is 45 to 75 MPa while Kb-1c is 45 to 85 MPa. KB-1b, the last trend in the load curve is 75 to 95 MPa where velocity is slowly decreasing. On the other hand, KB-1a and KB-1c fourth trend, velocity starting to decrease, begins from 85 to 116 MPa and the last trend for KB-1a is 116 to 138 MPa. The last trend for KB-1c in the load 120 to 156 MPa. The unload curve of KB-1b has three trends, 8 to 15 MPa, 15 to 46 MPa, and 46 to 96 MPa. KB-1a has four trends, 8 to 15 MPa, 15 to 38 MPa, 38 to 97 MPa, and 97 to 138 MPa. KB-1c has three trends, 8 to 45 MPa, 45 to 95 MPa, and 95 to 155 MPa.

The P-wave velocity load curve in the X-direction for KB-1b, KB-1a, and KB-1c all have 3 trends. The first trend for all samples are the same, 8 to 15 MPa. The second trend for KB-1b is 15 to 85 MPa. KB-1a's second trend starts from 15 to 65 MPa. The next trend for KB-1c is 15 to 105 MPa. The last trend for KB-1a and KB-1c are 105 to 138 MPa and 115 to 155 MPa. The first trend in the unload curve is similar for KB-1b and KB-1a in terms of the start and the end, 8 to 15 MPa. The second trend for KB-1b is 15 to 95 MPa. The last three trends for KB-1b is 15 to 27 MPa, 27 to 97 MPa, and 97 to 138 MPa. KB-1c first trend is 15 to 55 MPa, second trend 55 to 95 MPa, and third trend 95 to 155 MPa.

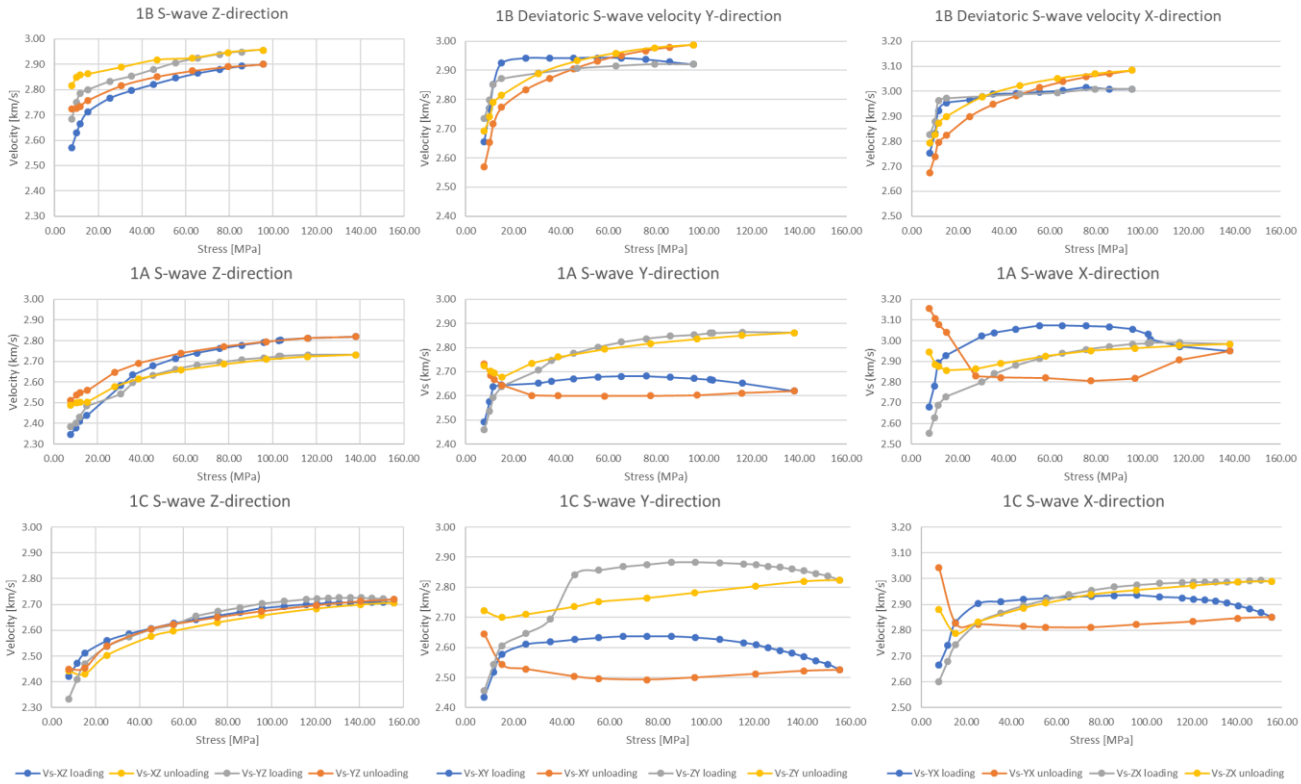

Figure 25 Shear wave velocity Z-direction (b), Y-direction (c), and X-direction (d) vs deviatoric stress plots for KB-1b, KB-1a, and KB-1c.

For sample KB-1b, signs of decrease of velocity only is shown in the XY- and YX-direction which starts at approximately 55 MPa and 75 MPa, respectively. As for sample KB-1a, in the XY- and YX-direction velocity decreases at around 75 and 65 MPa. While in the ZX- and ZY- direction for sample KB-1a, it starts to decrease at 116 MPa. Unlike KB-1b and KB-1a, sample KB-1c displays velocity decreasing in more directions compared to the other two samples. This is expected knowing that in P-wave velocity measurement, crack growth is clearly present. In the XY- and YZ- direction, velocity declines at 75 and 135 MPa. Meanwhile ZY- and YX- has the same stress point in velocity declination which is 95 MPa. At around 150 MPa ZX – and XZ – directions display velocity decrease.

In the unloading process, for the X-direction and the Y-direction for sample KB-1a and KB-1c there seems to show a sudden spike of velocity increasing happened almost at the end of the unloading process. To be precise, for sample Kb-1a, in the XY- and YX- direction the spike starts at 27 MPa, while in the ZY- and ZX-direction, the sudden increase in velocity begins at 15 MPa. Meanwhile for sample KB-1c, besides YZ-direction, the rest starts to spike up in velocity approximately 15 MPa. This means when all three pistons start to release stress, the new cracks start to immediately close

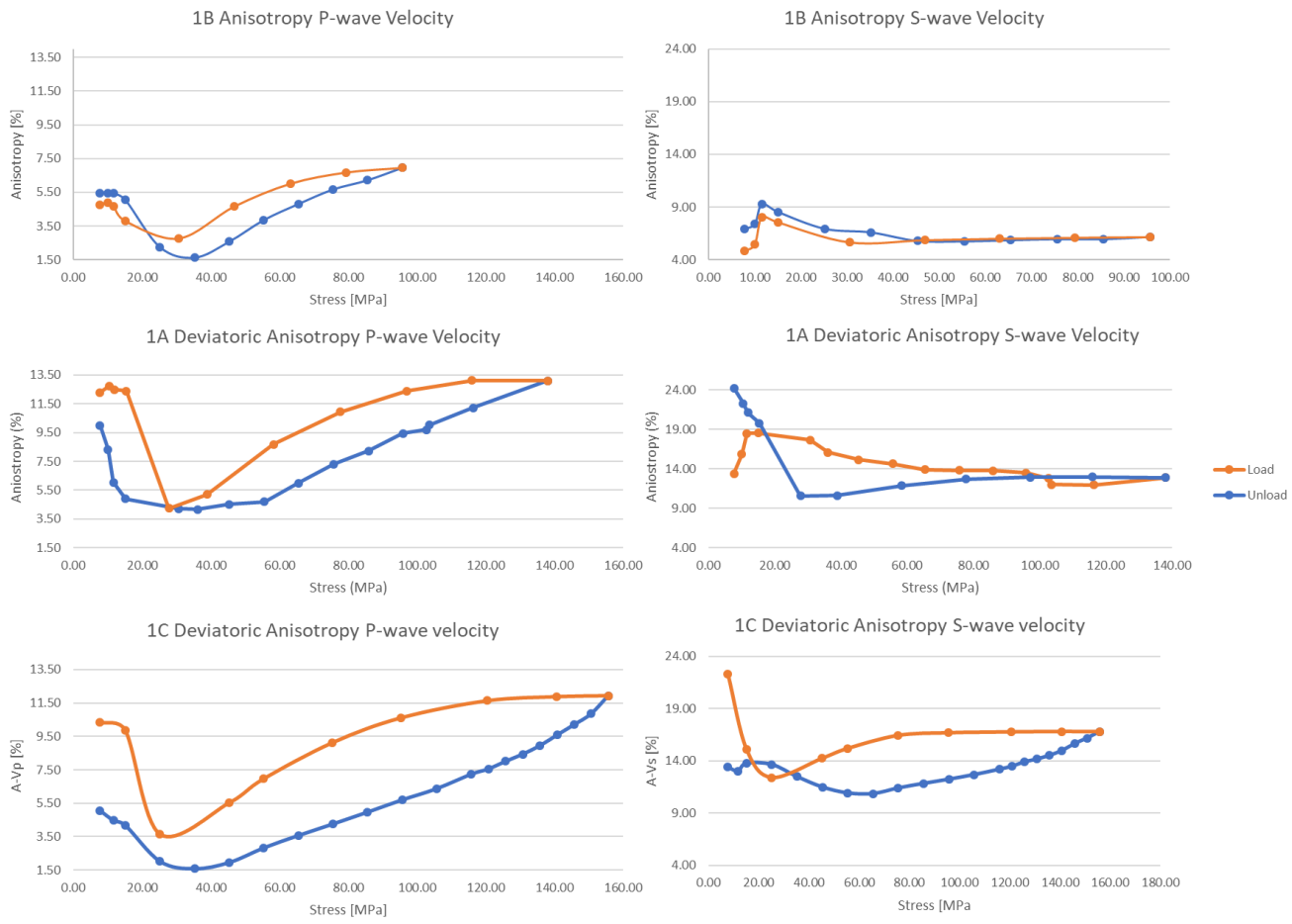

Figure 26 Anisotropy P-wave (left) and S-wave (right) vs deviatoric stress plots for KB-1b, KB-1a, and KB-1c. Blue dotted line represents the loading stress process and orange dotted line is the unloading process.

By looking at the anisotropy P-wave diagram for all three samples, the minimum point is between 25 – 36 MPa. This suggests that the microstructure in all three direction is similar. When the stress is released slowly, the P-wave anisotropy slowly decreases to a point it hits a minimum value between 25 – 30 MPa. The sudden increase of anisotropy is explained by the P-wave velocity measurement. The sample, based on the P-wave velocity data, suggests deformation, thus the sudden spike at the end. Sample KB-1c clearly displays a difference in anisotropy value compared to KB-1b and KB-1a whereas both of the sample reveals a slight contrast between the start of the loading and the end of the unloading process.

On the other hand, S-wave anisotropy diagrams shows a unique characteristic especially KB-1b whereas the trend for its loading and unloading process is quite different compared to KB-1a and KB-1c. The trend for the unloading process of sample KB-1b follows the pattern of the loading process. Moreover, the value after all stress is released presents a smaller value, though it is considered not significant, meaning that a few pores or pre-existing cracks have closed. Sample KB-1a and KB-1c is not quite different to one another,

both have minimum unloading points at 25 MPa and supports the present of new cracks existing within the samples. This is based on the end value where both has higher values compared to the start of the loading process. Sample KB-1a starts off from 13% to 24%. As for sample KB-1c, starts off from 13% to 22%.

3.2.2 Hydrostatic stress stage

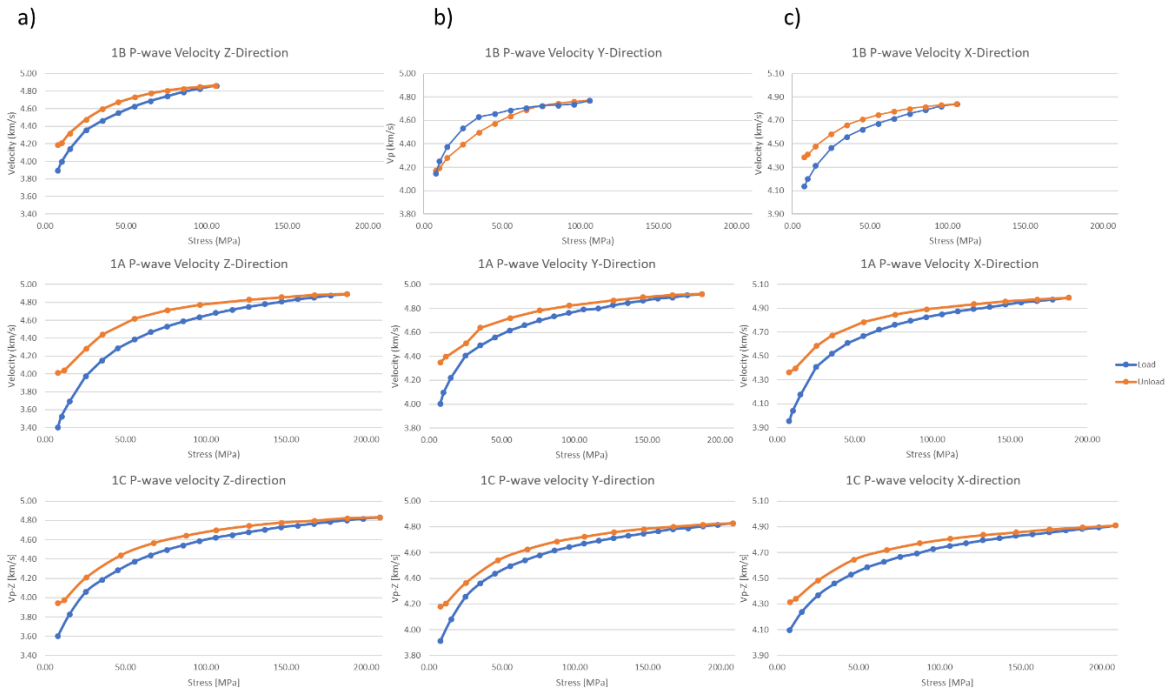

Figure 27 Compressional wave velocity Z-direction (b), Y-direction (c), and X-direction (d) vs hydrostatic stress plots for KB-1b, KB-1a, and KB-1c. Blue dotted line represents the loading stress process and orange dotted line is the unloading process.

For the P-wave velocity measurement, KB-1b in the Y-direction displays a different pattern in comparison to KB-1a and KB-1c in the same direction. The loading trend is higher compared to the unloading trend which starts to show clearly at around 66 MPa. However, the velocity at the end is still the same as at the beginning. On the other hand, besides KB-1b in the Y-direction, the unload curve of the rest of the samples apparently shows a similar pattern to the loading curve.

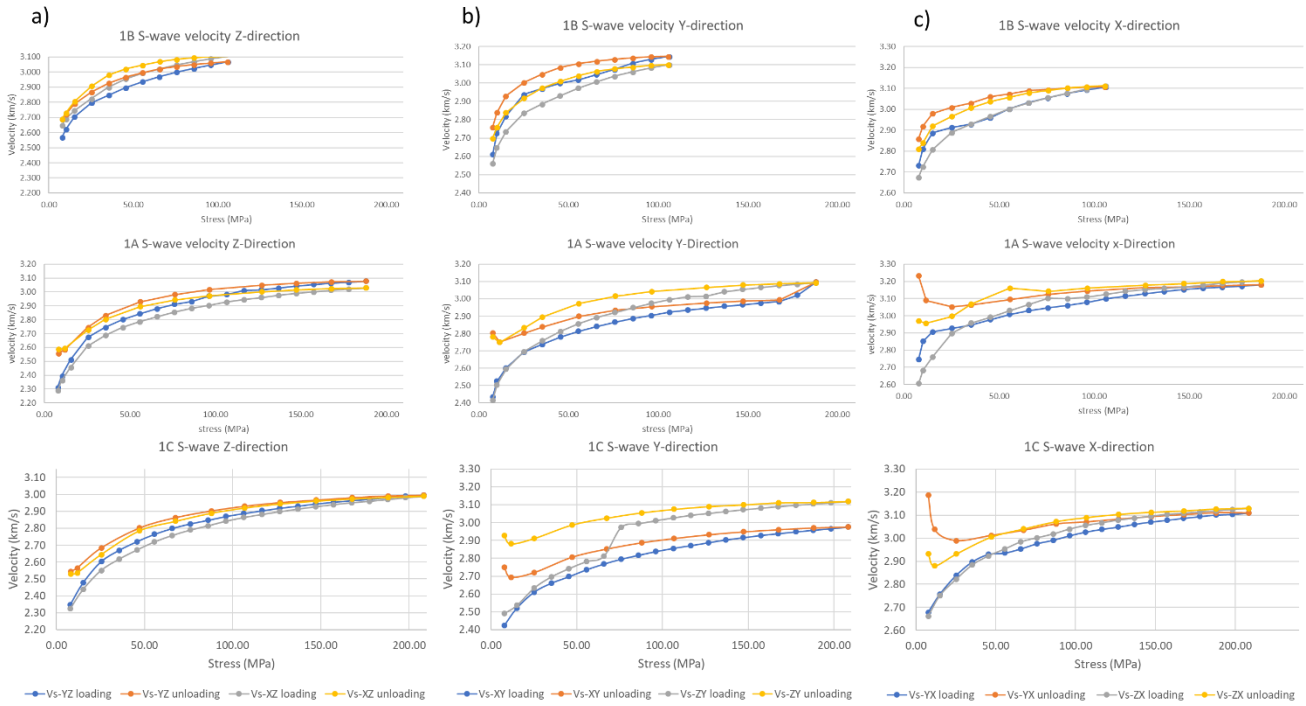

Figure 28 Shear wave velocity Z-direction (b), Y-direction (c), and X-direction (d) vs hydrostatic stress plots for KB-1b, KB-1a, and KB-1c.

The S-wave velocity diagram KB-1a and KB-1c in the Y-and X-direction appears to display that at around 25 MPa, a sudden increase of velocity. Though it is not quite significant, yet this helps in supporting the idea that at that direction, cracks tend to close.

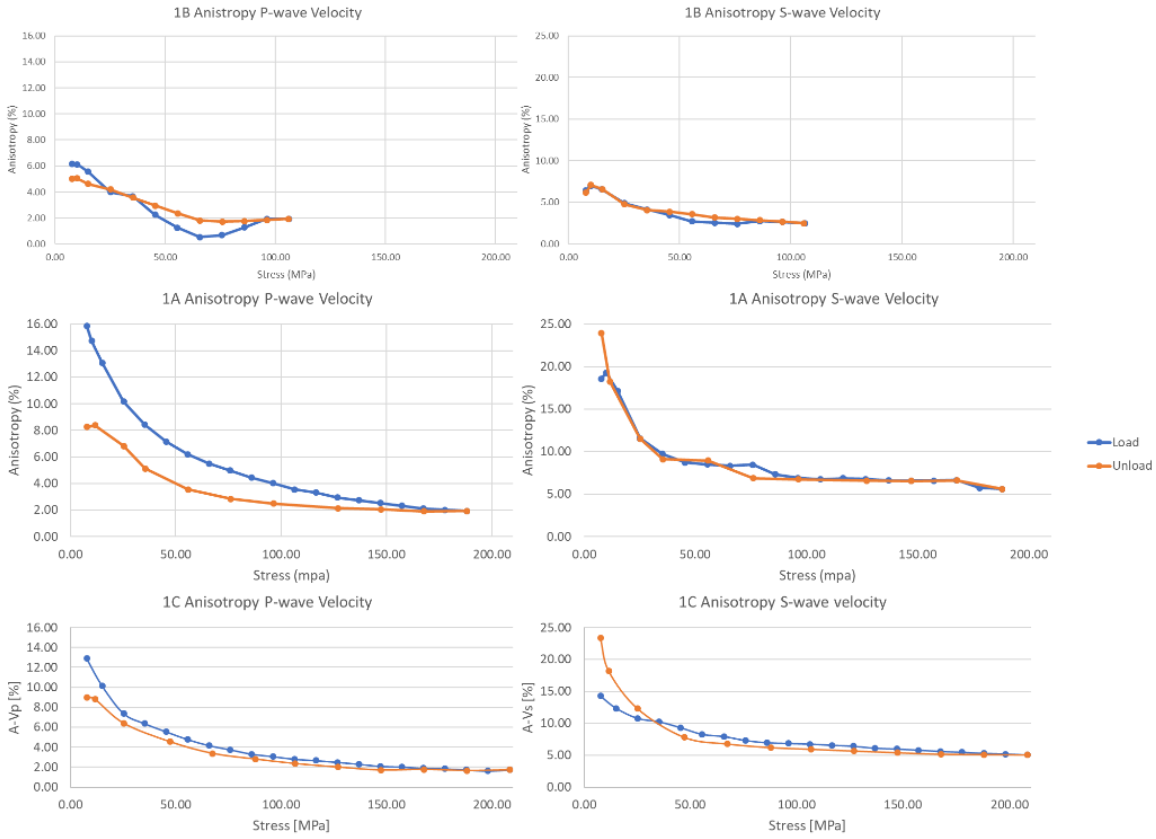

Figure 29 Anisotropy P-wave (left) and S-wave (right) vs hydrostatic stress plots for KB-1b, KB-1a, and KB-1c. Blue dotted line represents the loading stress process and orange dotted line is the unloading process.

3.3 Microstructural analysis

A thin section, 2 x 5 cm, was made of a sample of un-deformed Bebertal sandstone, taken from the same source as the three samples used in the deformation experiments. This is used for benchmarking the deformed sandstone, to compare and analyze the difference in crack growth. On the un-deformed sample, cracks which appear on the SEM image are mapped and calculated for the overall angle. Porosity estimation is also determined by calculating the black pixels, which represents the void/pore, divided by the total area of focus. Based on Figure 30, the red squares placed on the binary image are the area of focus for the pore estimation. The porosity calculation could not be done to the whole area because noises caused by dust which had stick on to the thin section causing black patches.

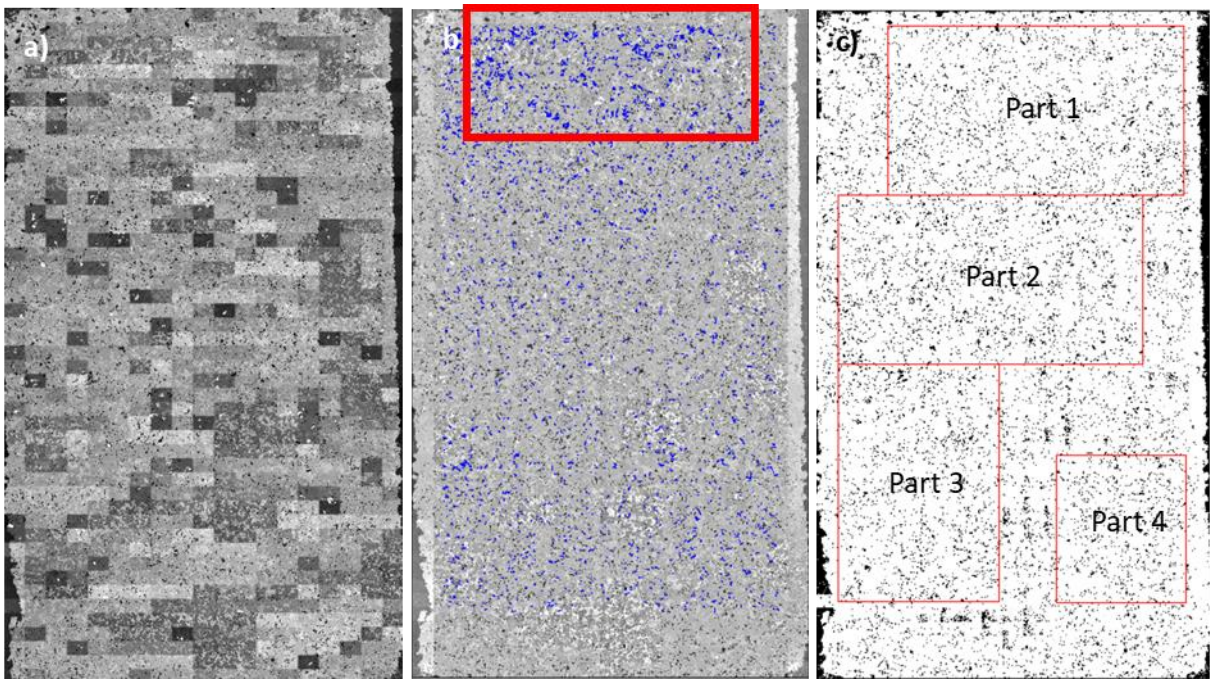

Figure 30 a) BSE image of a thin section of the un-deformed sample, b) grey contrast-leveling of the BSE image, the red square indicates an area with high crack density, c) binary image of the un-deformed sample, four red squares spread throughout the sample to estimate the porosity and crack density of the chosen areas.

The overall porosity of the thin section is approximately 5.8 – 6.6%. The total cracks that were mapped was 2592. Table 1 relays information of the crack orientation distribution throughout the un-deformed sample KB-01. The crack orientation with the most crack is within the range of 120 – 139 degrees with a total 340. Crack orientation within the range 80 – 99 degrees have the less number of cracks, 227 cracks.

Table 1 Crack orientation distribution of the un-deformed sample KB-01

CRACK ANGLE (DEGREE)	*TOTAL CRACKS*
0 - 19	281
20 - 39	305
40 - 59	276
60 - 79	267
80 - 99	227
100 - 119	295
120 - 139	340
140 - 159	320
160 - 179	281

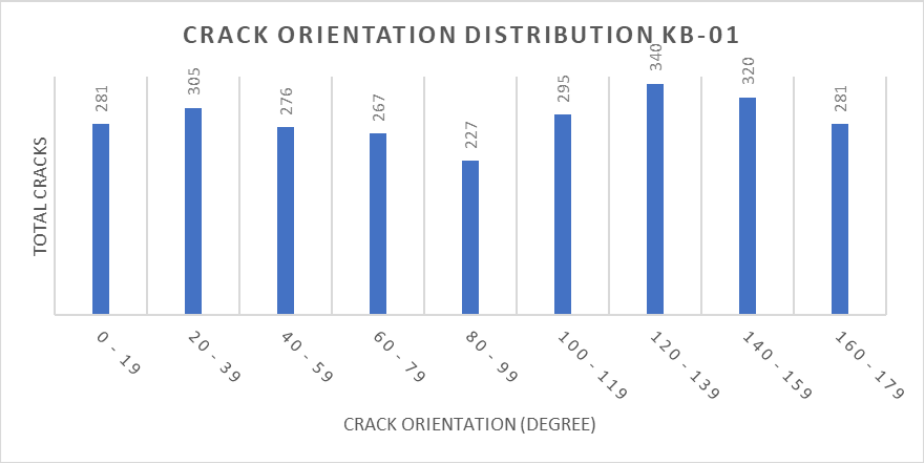

Figure 31 Crack orientation distribution of the un-deformed sample KB-01.

The average crack density of un-deformed sample KB-01 is 514.64 cm^{-2} with a maximum and minimum crack density of 807.72 and 339.93 cm^{-2}.

Table 2 Crack density vs porosity un-deformed KB-01

NAME	POROSITY (%)	CRACK DENSITY (CRACKS/CM^{-2})
PART 1	6.16	807.72
PART 2	6.60	339.93
PART 3	6.12	452.65
PART 4	5.80	458.25

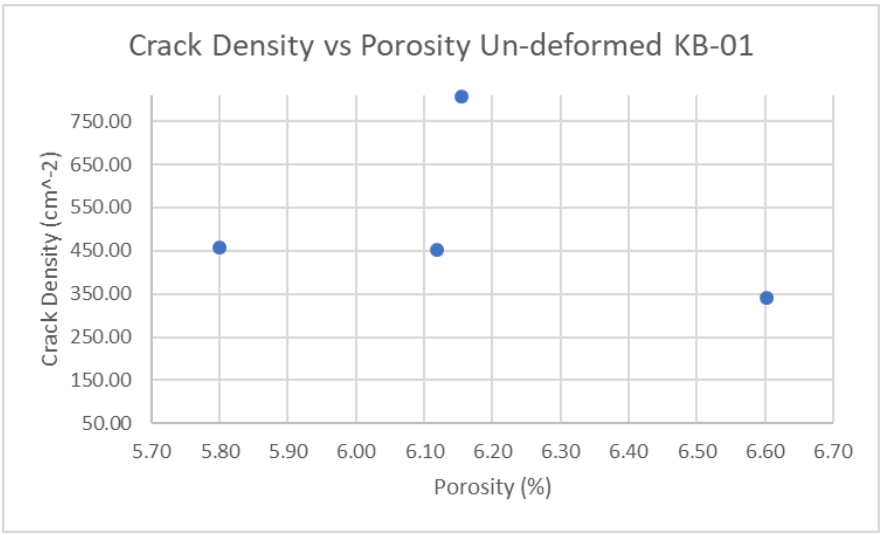

Figure 32 Crack density vs porosity of the un-deformed sample KB-01.

The BSE image obtained from the Scanning Electron Microscope (SEM) images for KB-1b had a low resolution (Figure 42) where the SEM scanned the whole thick section. The evaluation of the quality of

the image of KB-1b led to choose another way to gain a better-quality BSE image by shortening the scanned area for KB-1a and KB-1c (Figure 33).

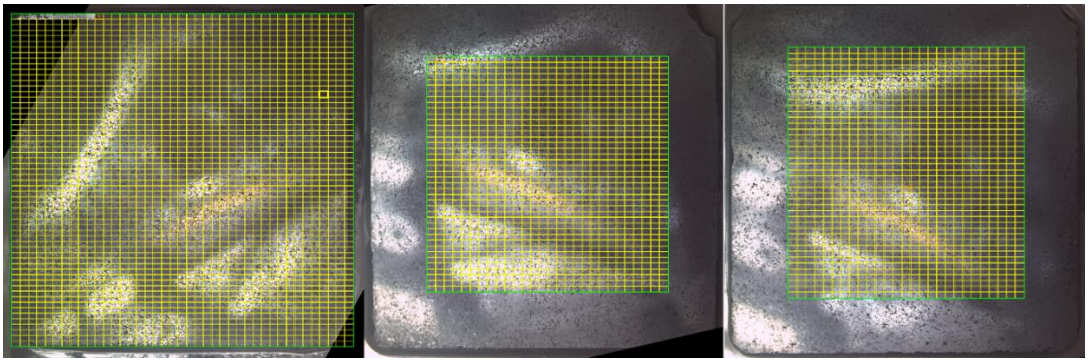

Figure 33 An image of the samples, KB-1b (left), KB-1a (middle), and KB-1c (right being scanned by the Scanning Electron Microscope (SEM). The yellows line covers the area of where the SEM scanned.

Because of KB-1b had a very large area to map out, the middle section of the image shown in Figure 34 is the focused area for mapping. The mapped area for sample KB-1b, KB-1a, and KB-1c is 4 x 2 cm, 2.7 x 2.7 cm, and 2.6 x 2.8 cm, respectively.

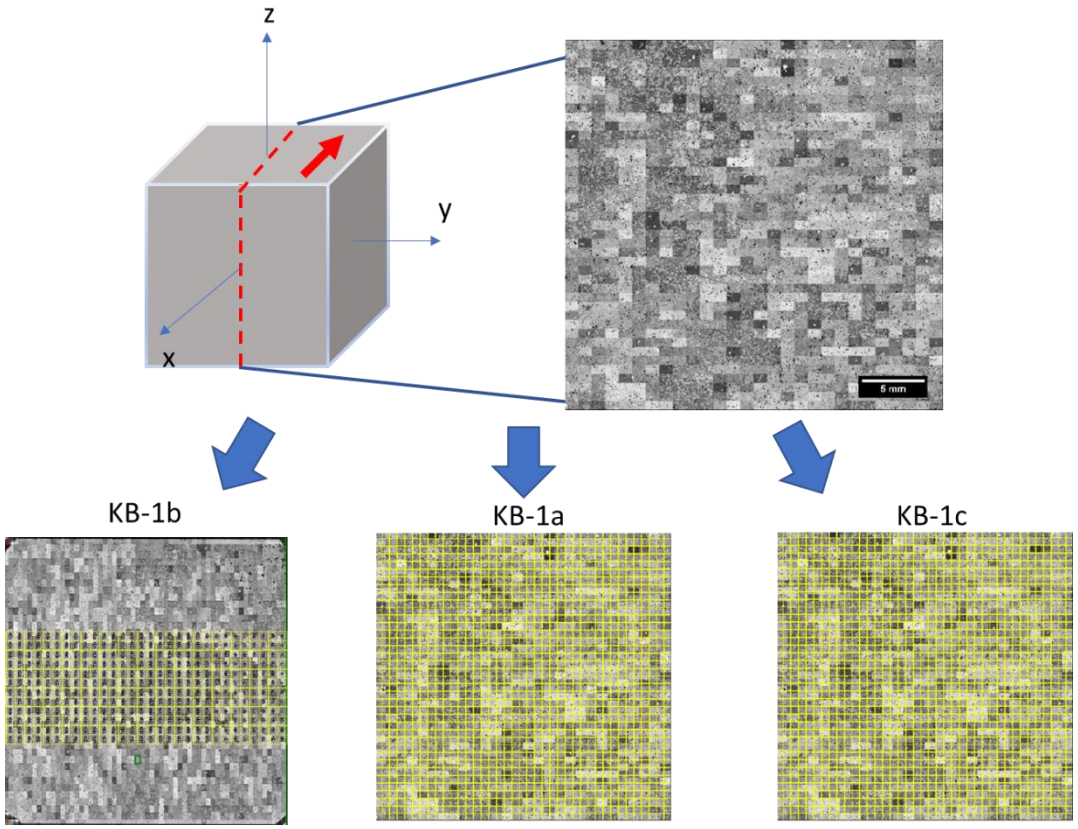

Figure 34 The mapped area for each sample, where for KB-1b was mapped throughout the middle section of the image (left), the whole image of KB-1a and KB-1c was mapped. The red dashed lines indicate where the plane was cut through the cube sample.

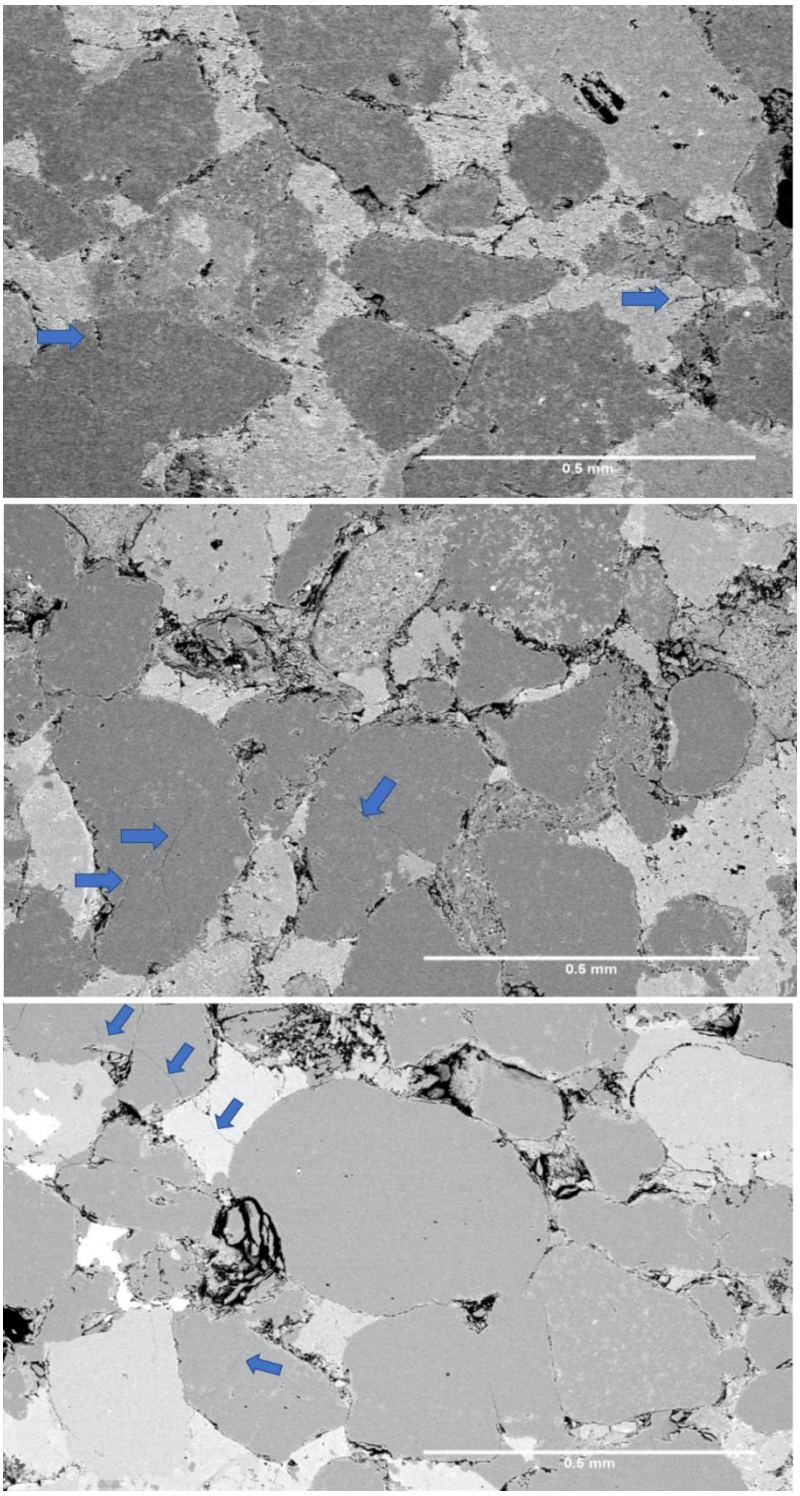

Figure 35 Mosaic tile of KB-1b (top), KB-1a (middle), and KB-1c (bottom). Blue arrows indicated cracks present within the grains.

Table 3 Crack Orientation distribution of sample KB-1b, KB-1a and KB-1c.

CRACK ORIENTATION	TOTAL CRACKS		
	KB-1b	KB-1a	KB-1c
0 - 19	5	106	102
20 - 39	9	85	102
40 - 59	11	84	92
60 - 79	14	79	90
80 - 99	6	83	82
100 - 119	3	103	100
120 - 139	10	98	72
140 - 159	3	87	78
160 - 179	10	83	90

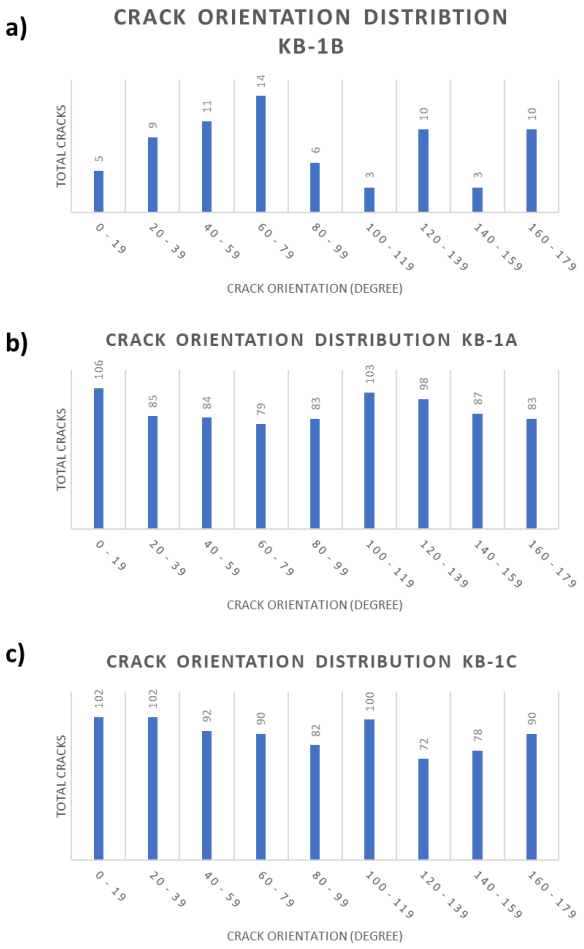

Figure 36 Diagrams of the crack orientation distribution of samples, which were deformed by going through deviatoric stress. a) KB-1, the maximum differential stress reached was 80 MPa; b) KB-1a, maximum differential stress reached was, 120 MPal; c) KB-1c, the maximum differential stress reached was 140 MPa.

Sample KB-1b had a maximum differential stress of 80 MPa which was referred to R. P. J. Pijnenburg MSc. experiment. At that differential stress, axial strain displayed a small deviation from linearity meaning primary pores and cracks are slowly closing with increasing compaction.

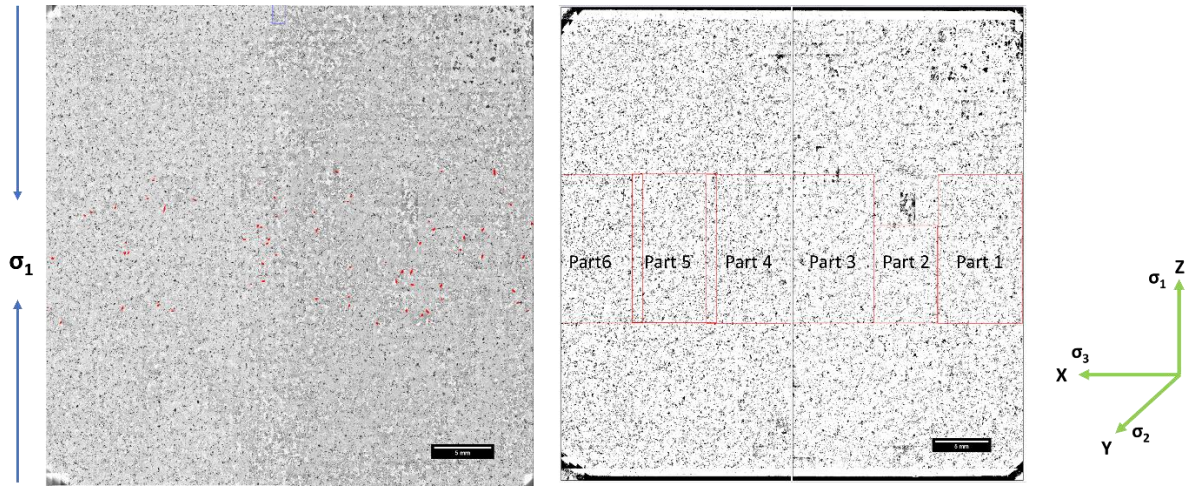

Figure 37 Cracks mapped in blue (left) and the chosen area (KB-1b) for crack density and porosity measurement. A sketch of the plane view in 3D of the three principle stresses.

A total of 71 cracks were mapped on KB-1b, much less than the un-deformed sample KB-01. The average crack density of KB-1b was 13.72 cm^{-2} with the highest 25.86 cracks/cm^{-2} and minimum 5.99 $cm^{-2.}$

Table 4 Porosity vs crack density of sample KB-1b

NAME	POROSITY (%)	CRACK DENSITY (CRACKS/CM^{-2})
PART 1	7.77	12.76
PART 2	7.32	25.86
PART 3	6.257	11.67
PART 4	8.7	14.97
PART 5	9.562	11.09
PART 6	8.749	5.99

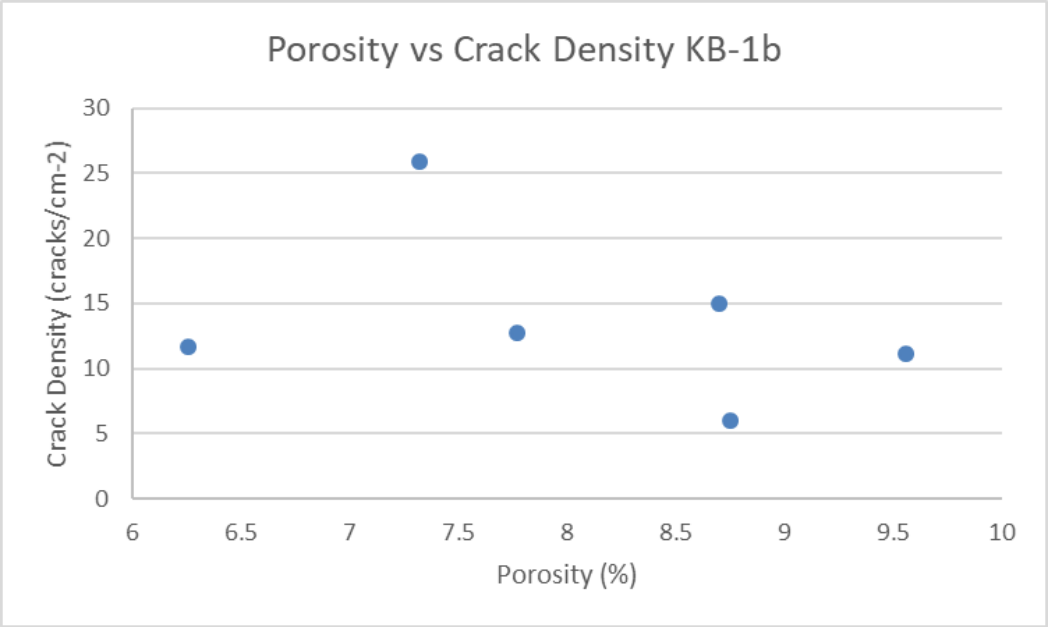

Figure 38 Crack density vs porosity of deformed sample KB-1b.

Sample KB-1a with a maximum differential stress of 120 MPa had total 808 cracks mapped within an area of 2.7 x 2.7 cm. The average crack density was 97.03 cracks/cm^{-2}, maximum 150.6 cracks/cm^{-2} and minimum 38.77 cracks/cm^{-2}.

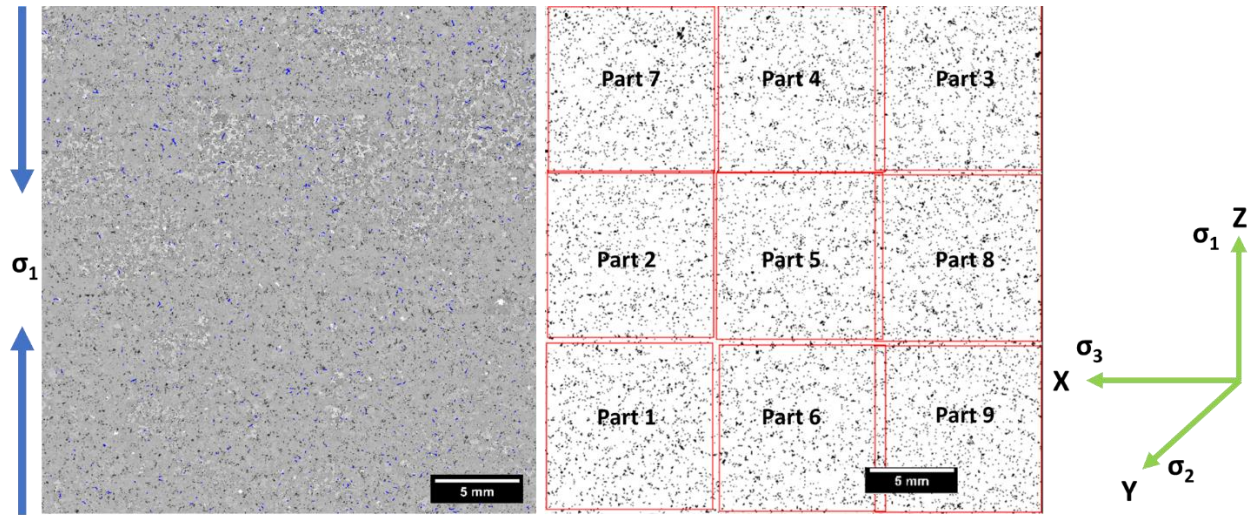

Figure 39 Cracks mapped in blue (left) and the chosen area (KB-1a) for crack density and porosity measurement. A sketch of the plane view in 3D of the three principle stresses.

Table 5 Crack density vs porosity of sample KB-1a

SECTION NAME	POROSITY	CRACK DENSITY (CRACK/CM^{-2})
PART 1	5.03	60.08
PART 2	4.61	38.77
PART 3	5.17	129.24
PART 4	4.83	101.03
PART 5	5.02	78.98
PART 6	5.21	89.17
PART 7	5.38	98.26
PART 8	5.29	150.60
PART 9	5.27	127.15

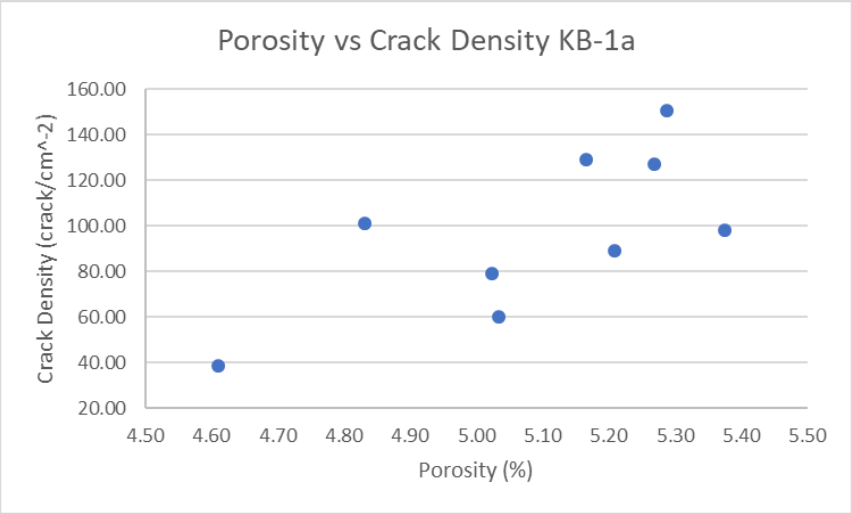

Figure 40 Crack density vs porosity of deformed sample KB-1a.

The range porosity based on the nine subareas is 4.61 – 5.38% and crack density, 38.77 – 150.60 crack/cm^{-2}.

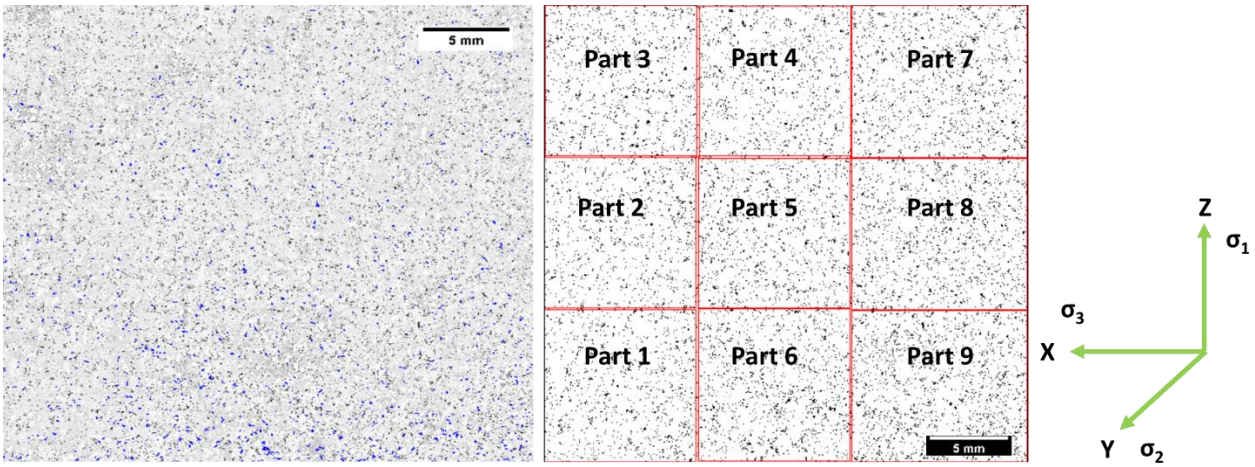

The last experiment, KB-1c with the highest differential stress, 140 MPa had total cracks of 1234. The average porosity is 5.02% in the range of between 4.34 – 6.20% and the average of crack density 145.60 cracks/cm^{-2} with the maximum 288.32 cracks/cm^{-2} and minimum 56.60 cracks/cm^{-2}.

Table 6 Crack density vs porosity of deformed sample KB-1c

NAME	POROSITY (%)	CRACK DENSITY (CM^-2)
PART 1	4.58	191.10
PART 2	4.34	92.49
PART 3	4.68	56.60
PART 4	4.49	64.39
PART 5	4.90	116.87
PART 6	5.67	282.53
PART 7	5.08	87.74
PART 8	5.25	130.38
PART 9	6.20	288.32

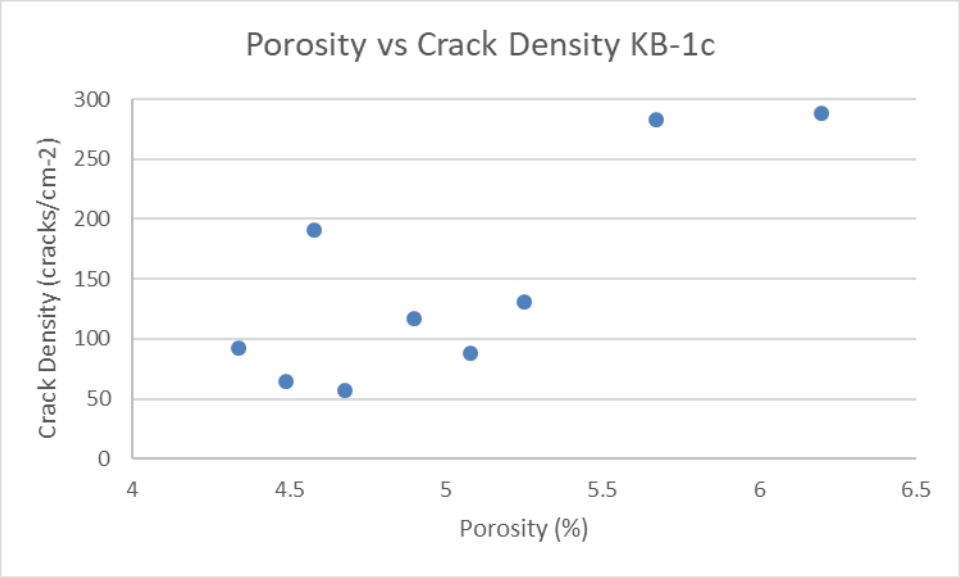

Figure 41 Crack density vs porosity of deformed sample KB-1c

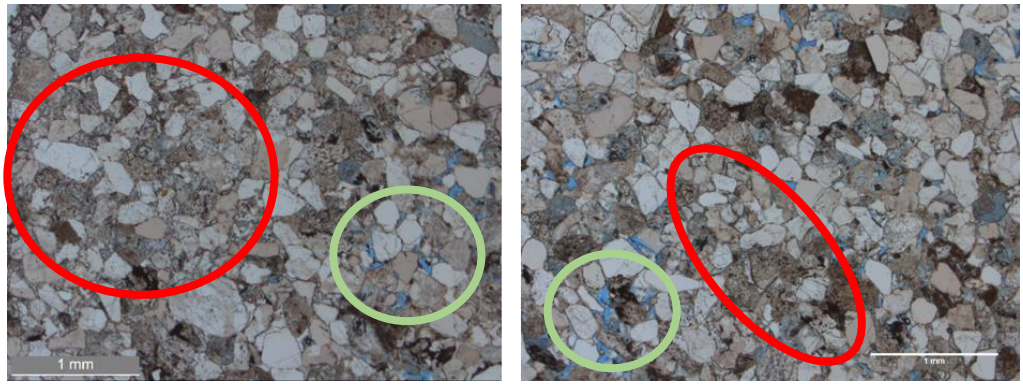

Figure 42 Microscopic images of the un-deformed samples KB-01. Green circles show the pores and the red circles indicate framework minerals where clays or lithic fragments tend to fill in between quartz, K-feldspar

Thin sections of the un-deformed sample were one of the references used to help in identifying minerals for the Multi-Otsu thresholding. Based on the thin sections, mineral quartz mostly makes up the un-deformed sample. The quartz made up to rounded – well rounded grains. There were many lithic fragments or clays which filled in between minerals (Figure 42). The mineral content of sample was calculated using the Multi-Otsu Thresholding which the mineral content is stated in Table 7.

Table 7 Mineral content of the Bebertal sandstone using Multi-Otsu Thresholding

MINERALS	MINERAL CONTENT (%)
QUARTZ	64.40
BARITE	3.32
K-FELDSPAR + BARITE + CALCITE	17.72
K-FELDSPAR + CEMENT + LITHIC FRAGMENT	16.86
CLAY	4.32

Chapter 4. Discussion

Reservoir compaction has many factors effecting the reservoir which one of them is grain cracking (Hol et al., 2015). True triaxial stress apparatus was used to induce new cracks within the grain while being observed by measuring elastic waves in three principal axis, Z, Y and X direction.

The strain data at 8 to 15 MPa, which $\sigma_1 = \sigma_2 = \sigma_3$, of sample KB-1b, KB-1a, and KB-1c in all three principal axis, displays trend increasing. An increasing trend in the axial strain indicates shortening on the three principal axis. The volumetric strain data with a stress range between 8 to 15 MPa supports the idea of the sample being compact. Evidence show that P-wave and S-wave at that stress point displays an increase

of velocity. This implies that some pre-existing pores and cracks are slowly closing with the increase of compaction when nearly in hydrostatic stress (Alkan et al., 2007).

After 15 MPa, the deviatoric loading begins ($\sigma_1 > \sigma_2 = \sigma_3$), the axial strain in the Z-direction implies shortening as the axial stress is increased. Volumetric strain after 15 MPa indicates a slow compaction occurring with trend increasing. In the Y and Z direction, the axial strain displays different behavior after 15 MPa. For all samples, in the Y and Z direction the data implies that dilation is occurring with a trend that slowly decreases as the vertical stress is increased. In the Y- direction, the P-wave velocity increases until 75 MPa for KB-1b and KB-1a, and 85 Mpa for KB-1c while the one of the S-wave velocity starts to decrease at of 75 MPa. This indicates that even if the axial strain data in the Y and Z direction implies the sample is extending until it reaches the maximum differential stress, this does not mean that the velocity follows through. Instead the P-wave and the S-wave velocity increases until a certain point of stress, then decreases until stress reaches maximum differential stress. This is defined as *plastic behavior* where cracks continue to grow as stress increases and volumetric strain also increase (Alkan et al., 2007)

In the Z-direction for all three samples for the P-wave and S-wave velocity data, there are no declination in trend which means the samples incline to compact. There is no indication of cracks opening in the Z-direction. Sample KB-1b is likely to not have new cracks based on the P-wave and strain data. Even though the P-wave velocity in the Y- and X -direction, at 85 MPa starts to decrease it is unlikely to see new cracks appearing. This is proven by the crack mapping of KB-1b.

The axial strain data in the Z, Y and X direction after fully unloaded implies that there happens to be a permanent axial strain, supported by the volumetric strain data. This indicates that all three samples have permanent deformation. Even though in the Y-direction of KB-1c did not show any changes, however in the other directions claim to show there happens to be a change in volume.

In the P-wave and S-wave velocity data, after 15 MPa in the Y and Z direction, for sample KB-1a and KB-1c the velocity increases slowly which indicates that the cracks are slowly closing but not as much as before 15 MPa. The slowly increase in velocity after 15 MPa shows a behavior of the difficulty of cracks being 'completely' closed.

Approximately at 85 MPa for KB-1a in the Y- and X- direction and for KB-1c only in the Y- direction, velocity starts to decrease. In the X- direction for KB-1c, velocity starts to decline at around 105 MPa. This implies that new cracks have developed at this stage. This might also explain the reason behind the cracks distribution along sample KB-1a and KB-1c. Sample KB-1c had a higher stress point for new cracks to

appear, while KB-1a is lower. To have a better distribution of cracks, higher stress applied on to the sample, is to be done for KB-1c.

In the unloading process of the P-wave velocity, sample KB-1c shows a promising result of a sample containing new cracks and well permanently deformed sample. This is proven by observing the curve in the unloading process where it does not follow up the loading process curve, but stays relatively horizontal linear. Sample KB-1a somewhat has similar pattern in trend to KB-1c in the unloading cycle, however at 27 MPa, the velocity starts to increase again. This indicates that new cracks that have been produced in the loading process have started to close at around 27 MPa for both in the Y- and X- direction. Meanwhile, KB-1c does also show a behavior of new cracks closing at around 55 MPa, but not quite as significant as KB-1a.

S-wave velocity decreases in various stress points since there are 6 shear wave velocities however it depends on maximum differential stress. KB-1b only have two shear wave velocities which decreased as stress increases, KB-1a has four and KB-1c has six. This states that the higher the differential stress, the more new cracks tends to increase in various directions (Browning et al., 2015). This does not apply only for S-wave velocity, but also P-wave velocity.

In previous statement, KB-1b is stated to might not have new cracks developed in the loading process. This is proven not just by analyzing the P-wave and S-wave velocity diagram, but also from the S-wave anisotropy.

When hydrostatic stress was applied to the sample, the axial strain and volumetric strain shows shortening and compaction which indicates that cracks, formed due to the deviatoric stress, partially are closed because of the applied stress from all six directions. P and S-wave velocities measurement shows that there happens to be slightly higher velocity compared to the beginning of the load cycle which can be assumed that the cracks made from the deviatoric stage are partially closed. Unfortunately, to point out the maximum stress achieved in the deviatoric stress is quite difficult. For an example, the load rate of the P-wave velocity for hydrostatic stress stage in the Y-direction, at 45 MPa for KB-1b indicates the start of when cracks are assumed to be quite difficult to close, KB-1a starts at 55 MPa and KB-1c starts at 75 MPa. Overall with the hydrostatic stress method, it is quite difficult to determine the state of stress of previous deformation.

Crack mapping is a method where it is quite difficult if the definition of cracks per case is not absolute There were problems regarding crack mapping and one of them were reproducing the same crack map.

An individual must be experienced to reproduce a crack map that is 90% similar to original map. The problem that occurred during the crack mapping was the difficulty in mapping cracks when the images were in low resolution. One of the example is image KB-1b, first attempt of crack mapping it was over 2000 cracks, second time it was over 400, the third stated in the Result chapter, 71 cracks. Thus, crack mapping is basically the consistency of defining of what a crack is. Besides the difficulty due to low resolution is when measuring the porosity of the whole area. The binary image of KB-1b is one of the results where there happens to be patches in some areas of the image.

For future research, the sample used in this experiment had very dense porosity compared to the Groningen gas reservoir, hence it would be better to use rock samples that have the same range porosity as the Groningen gas field, much more porous such as Slochteren sandstone. The experiment in Kiel used room temperate when the sample went through deviatoric and hydrostatic. It would be better if the temperature was the same as the reservoir, thus it would be easier to compare the results. In this experiment, the hydrostatic stress method was used to see whether this method could be used to estimate the stress that initiated the deformation where $\sigma_1 = \sigma_2 = \sigma_3$. Instead of $\sigma_1 = \sigma_2 = \sigma_3$, a new method where σ1 stays constant while σ2 and σ3 changes could help in determining the state of stress. This study case, relation between crack density and porosity was investigated. However, there were not much to say since porosity range was quite small. For this particular sandstone, it would be better to investigate relation between crack density clay content and porosity to understand more what effects the higher number of cracks.

Chapter 5. Conclusion

The true triaxial stress recreates the situation similar to the real field, however downscaled. The deformed samples which was performed using the true triaxial stress cannot be used to relate to the Groningen gas field because of the methods used were mostly done in room temperature and the sample itself apparently is low porosity. The mechanical data, axial strain and volumetric strain measurement are not able to stand alone in determining the precise stress point of the crack growth, however with the compressional and shear wave velocity measurement, it is easier to pinpoint the stress of when crack appears. While deviatoric stress induces crack growth, hydrostatic stress apparently does not create new cracks, but attempts to close cracks. However, even though hydrostatic stress method is to close up cracks, apparently, it was unable to pinpoint the state of stress before deformation. This might be because

the stress path was different to the stress path of the deviatoric stress. Hence, hydrostatic stress is not able to point out the in-situ state of stress.

References

Alkan, H., Cinar, Y., & Pusch, G. (2007). Rock salt dilatancy boundary from combined acoustic emission and triaxial compression tests. International Journal of Rock Mechanics and Mining Sciences, 44(1), 108-119.

Browning, J., Meredith, P. G., Stuart, C. E., Healy, D., Harland, S., & Mitchell, T. M. (2017). Acoustic characterization of crack damage evolution in sandstone deformed under conventional and true triaxial loading. *Journal of Geophysical Research: Solid Earth*.

Fischer, C., Dunkl, I., von Eynatten, H., Wijbrans, J. R., & Gaupp, R. (2012). Products and timing of diagenetic processes in Upper Rotliegend sandstones from Bebertal (North German basin, Parchim Formation, Flechtingen high, Germany). Geological Magazine, 149(5), 827-840.

Gast, R. (1991). The perennial Rotliegend saline lake in NW Germany. *Geologisches Jahrbuch A*, *119*, 25-59.

Gast, R., Dusar, M., Breitkreuz, C., Gaupp, R., Schneider, J. W., Stemmerik, L., Geluk, M., Geissler, M., Kiersnowski, H., Glennie, K., & Kabel, S. (2010). Rotliegend. *Petroleum Geological Atlas of the Southern Permian Basin Area*, 101-121.

Hol, S., Mossop, A. P., Van der Linden, A. J., Zuiderwijk, P. M. M., & Makurat, A. H. (2015). Long-term compaction behavior of Permian sandstones-An investigation into the mechanisms of subsidence in the Dutch Wadden Sea. In *49th US Rock Mechanics/Geomechanics Symposium*. American Rock Mechanics Association.

Kern, H. (1982). P-and S-wave velocities in crustal and mantle rocks under the simultaneous action of high confining pressure and high temperature and the effect of the rock microstructure. *High-Pressure Researches in Geoscience*, 15-45.

Kern, H., Liu, B., & Popp, T. (1997). Relationship between anisotropy of P and S wave velocities and anisotropy of attenuation in serpentinite and amphibolite. *Journal of Geophysical Research: Solid Earth*, *102*(B2), 3051-3065.

Kern, H., Popp, T., Gorbatsevich, F., Zharikov, A., Lobanov, K. V., & Smirnov, Y. P. (2001). Pressure and temperature dependence of V P and V S in rocks from the superdeep well and from surface analogues at Kola and the nature of velocity anisotropy. Tectonophysics, 338(2), 113-134.

Kern, H., (2011). Measuring and Modeling of P- and S-Wave Velocities on Crustal Rocks: A Key for the Interpretation of Seismic Reflection and Refraction Data. *International Journal of Geophysics 2011*.

Klein, E., Baud, P., Reuschlé, T., & Wong, T. F. (2001). Mechanical behaviour and failure mode of Bentheim sandstone under triaxial compression. Physics and Chemistry of the Earth, Part A: Solid Earth and Geodesy, 26(1-2), 21-25.

KNMI. Aardbevingen Door Gaswinning in Noord-Nederland. Retrieved from: http://www.knmi.nl/cms/content/22993/aardbevingen_door_gaswinning_in_noord-nederland. 2013.

KNMI. Geïnduceerde aardbevingen in Nederland. Retrieved from: http://www.knmi.nl/seismologie/geinduceerde-bevingen-nl.pdf. 2013.

Kulke, H., Gast, R., Helmuth, H., & Lützner, H. (1993). Harz Area, Germany: typical Rotliegend and Zechstein reservoirs in the Southern Permian Basin (Central Europe). In *Field Trip 4, AAPG International Conference & Exhibition, The Hague, October 1993*.

Liao, P.-S., T.-S. Chen and P.-C. Chung. (2001). A fast algorithm for multilevel thresholding. *J. Inf. Sci. Eng.*17: 713-727.

Menke, W., & Levin, V. (2003). The cross-convolution method for interpreting SKS splitting observations, with application to one and two-layer anisotropic earth models. *Geophysical Journal International*, *154*(2), 379-392.

Nederlandse Aardolie Maatschappij (NAM). (2016). Study and Data Acquisition Plan Induced Seismicity in Groningen: Update Post-Winningsplan 2016. *147*.

Schröder, L., Plein, E., Bachmann, G. H., Gast, R. E., Gebhardt, U., Graf, R., Helmuth, H. J., Pasternak, M., Porth, H., & Süssmuth, S. (1995). Stratigraphiche Neugliederung des Rotliegend im Norddeutschen Becken. *Geologisches Jahrbuch* A *148, 3–21*.

Thienen – Visser, K. and Breunese, J. N. (2015). Induced Seismicity of the Groningen Gas Field: History and Recent Developments. *The Leading Edge, 34 (6), 664 – 666, 666 – 668, 670 – 671.*

Ziegler, P. A. (1990). Geological atlas of western and central Europe. Geological Society of London.

Acknowledgement

Alhamdulilah, I thank Allah for all the great chances He has given to me through my life. I thank my parents, Taufan Marhaendrajana and Dite Widiastuti for always supporting and encouraging me to never give up. I thank my supervisors, Prof. Dr. Christopher Spiers, Dr. Bart Verbrene, and Dr. Suzanne Hanax for always helping me in my master thesis project and always lifting my spirit up whenever I feel down. I thank my dear friend Veronica Donadio who always supports me from behind and helped me when I am a bit confused about life. I am grateful to my best friend, Annisa Noyara Rahmsary and all my friends who have been teasing me and trying make my life as crazy as possible.

Big thanks to Ronald P. J Pijnenburg who has helped in providing data of the conventional triaxial stress, helped in shaping the Bebertal sandstone to be delivered to Kiel, accompanying me to talk to Leonhard about the deformed cubes and many more. I thank Dr. Bahadur Motra for supervising me while I was observing the true triaxial stress appartus in Kiel. Last but not least, big appreciation to my sponsor, LPDP (Indonesian Endowment fund for education) who has sponsored me for two years while I was studying in the Netherlands. Once again, thank you.

Appendix

- Crack map of KB-1b, polygon lines were widened to 150

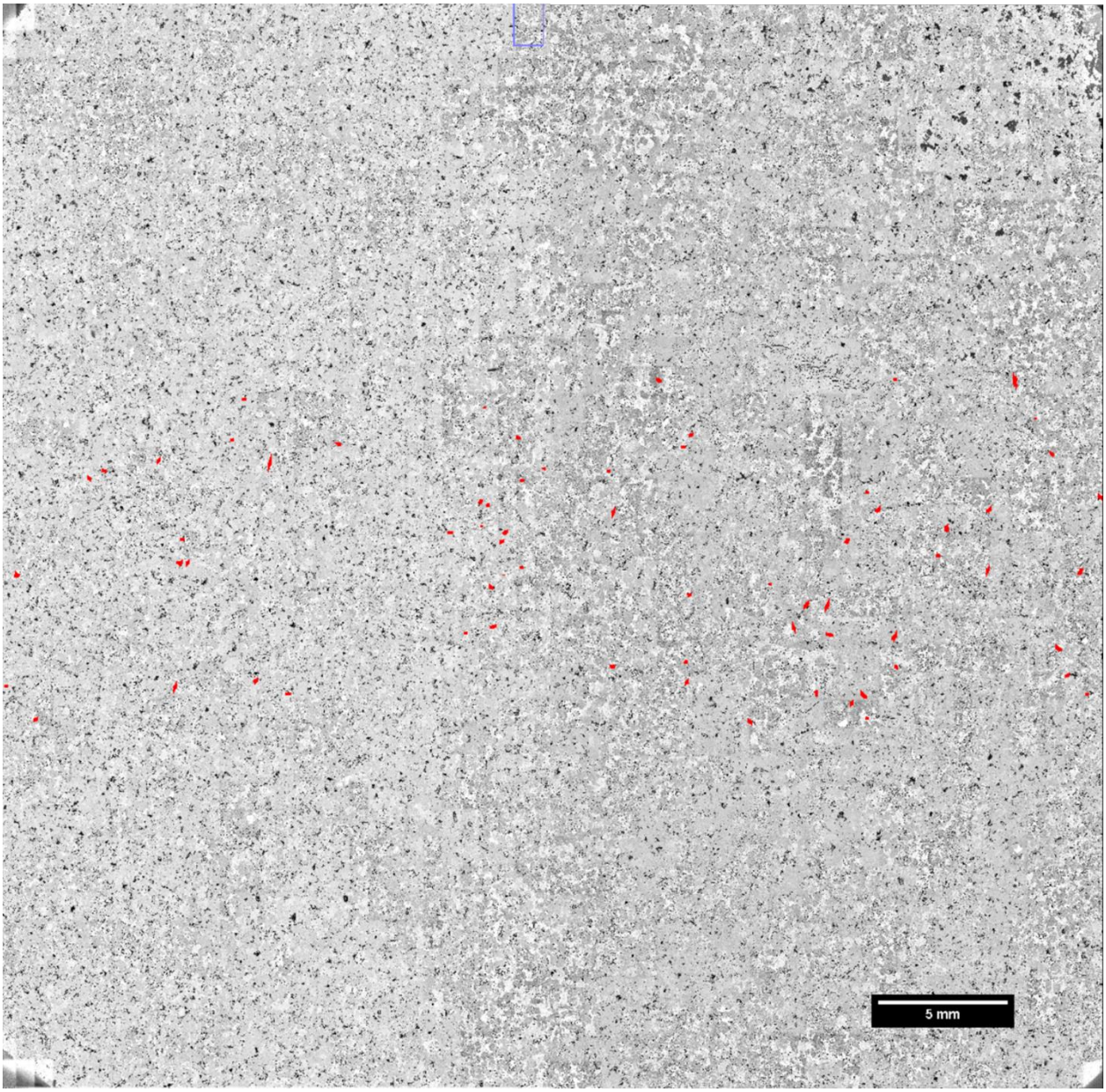

- Crack map of KB-1a, the polygon lines were widened to 150.

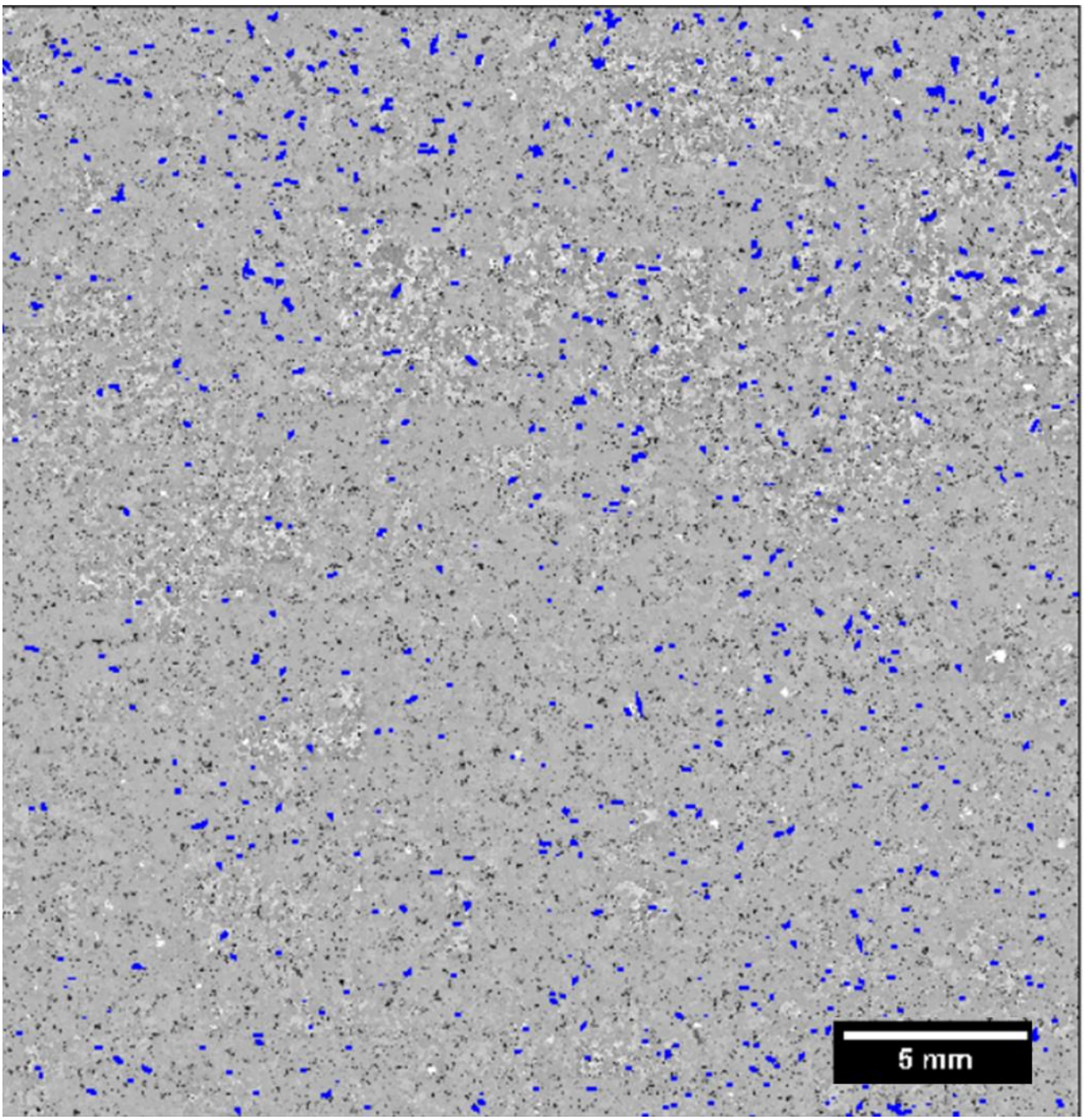

- Crack map of KB-1c, the polygon lines were widened to 100.

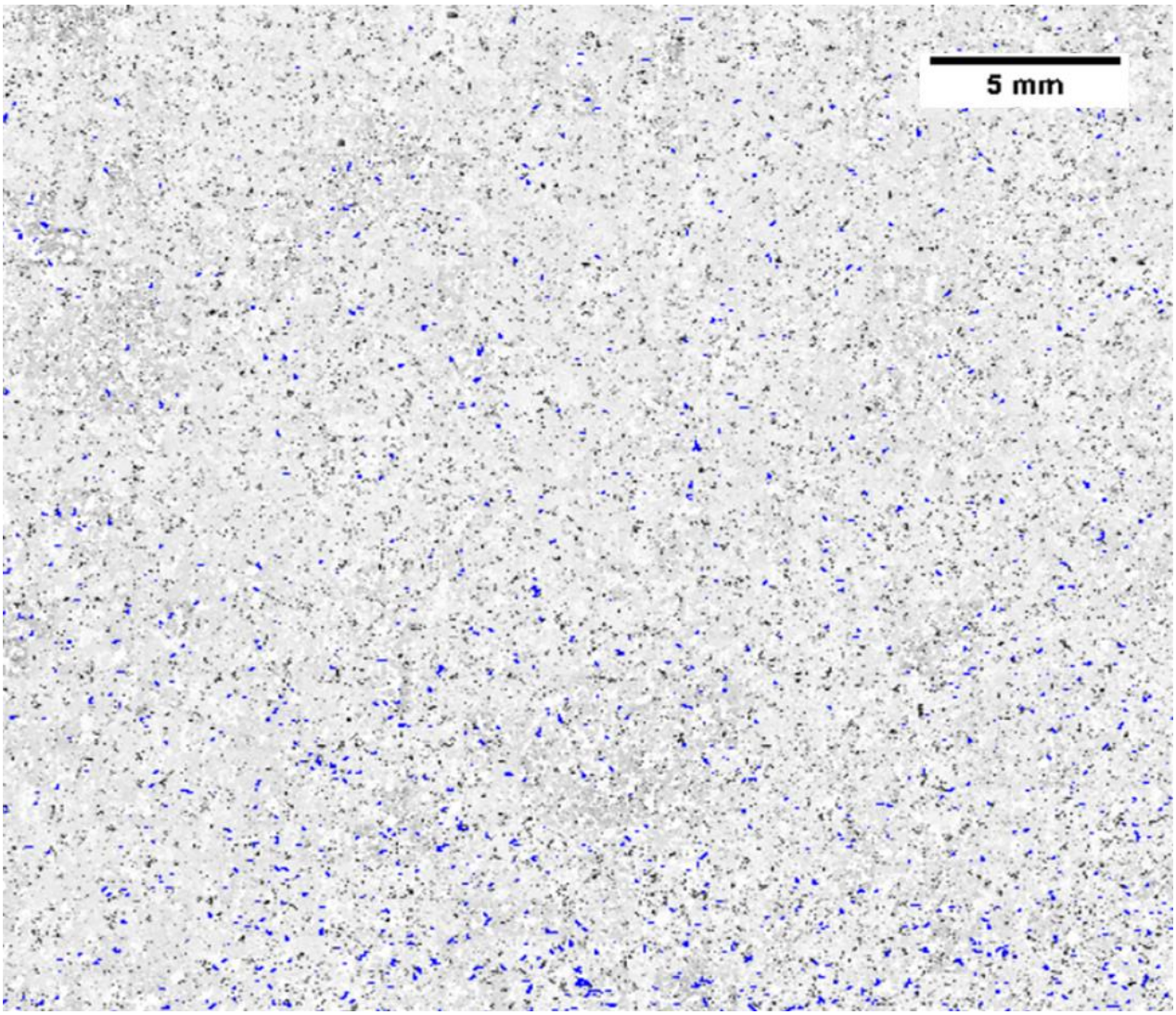
5 mm